Available online at www.sciencedirect.com

SciVerse ScienceDirect

Ceramics International 38 (2012) 3907–3927

CERAMICS INTERNATIONAL

www.elsevier.com/locate/ceramint

Compilation of mechanical properties for the structural analysis of solid oxide fuel cell stacks. Constitutive materials of anode-supported cells

Arata Nakajo [a,b,*], Jakob Kuebler [c], Antonin Faes [d], Ulrich F. Vogt [c], Hans Jürgen Schindler [c], Lieh-Kwang Chiang [e], Stefano Modena [f], Jan Van herle [a], Thomas Hocker [b]

[a] *Laboratoire d'Energétique Industrielle (LENI), Institut de Génie Mécanique, Ecole Polytechnique Fédérale de Lausanne, 1015 Lausanne, Switzerland*
[b] *ZHAW Zürich University of Applied Sciences, Institute of Computational Physics, CH-8401 Winterthur, Switzerland*
[c] *Empa, Swiss Federal Laboratories for Materials Science and Technology, 8600 Dübendorf, Switzerland*
[d] *Design and Materials Unit, University of Applied Science Western Switzerland, CH-1950 Sion, Switzerland*
[e] *Nuclear Fuel and Material Division, Institute of Nuclear Energy Research, Lung-Tan 325, Taiwan*
[f] *SOFCpower S.r.l.v., Al Dos de la Roda, 60, 38057-I Pergine Valsugana (TN), Italy*

Received 1 November 2011; received in revised form 6 January 2012; accepted 15 January 2012
Available online 25 January 2012

Abstract

The mechanical failure of one cell is sufficient to lead to the end of service of a solid oxide fuel cell (SOFC) stack. Therefore, there is growing interest in gaining knowledge on the mechanical properties of the cell materials for stress analysis.

This study compiles available data from the literature on the mechanical properties of the most common materials used in intermediate-temperature anode-supported cells: nickel and yttria-stabilized zirconia (Ni–YSZ) anodes, YSZ electrolytes, yttria (YDC) or gadolinia-doped ceria (GDC) compatibility layers and lanthanum strontium manganite (LSM) or lanthanum strontium cobalt ferrite (LSCF) cathodes. The properties for the simulation of stresses, i.e. coefficient of thermal expansion (CTE), Young's modulus, Poisson's ratio, creep behaviour and strength are reported, with an emphasis on temperature and porosity dependence and the evolution upon aging or cycling when available. Measurements of our Ni(O)–YSZ anode material includes the CTE (oxidised and reduced state), Young's modulus and strength at room temperature (oxidised and reduced) and 1073 K (oxidised).

Keywords: C. Creep; C. Mechanical properties; C. Strength; C. Thermal expansion; Solid oxide fuel cell

1. Introduction

Structural reliability of solid oxide fuel cells (SOFC) is a salient issue, which currently impedes their large-scale commercialisation. The in-series assembly of the single repeating units (SRU) to build a stack and the use of brittle ceramic materials for the manufacturing of the cells are striking weaknesses. The mechanical failure of one single cell usually quickly leads to the end of life of the stack, as it induces a succession of detrimental effects that act in a coupled manner. For instance, delamination or cracking of the electrode layers breaks the ionic and/or electronic conduction paths to the reaction sites. The ensuing local loss of performance induces a harmful redistribution of the current density [1,2]. Once cracked, the electrolyte does not any longer ensure the separation of the fuel and air compartments to the fullest extent. The local and unsteady combustion provokes a local increase of the temperature, as well as diverse chemical alterations of the cell layers, such as the reduction and re-oxidation (redox) of the nickel in the composite anode and the reduction of the cathode material [3]. All these undesirable chemical and electrochemical phenomena promote in turn additional stresses, which reach critical values in an accelerated manner.

SOFC stacks with a few hours of operation can fail because of improper control strategy. They incur in the longer term repeated full or partial thermal cycles and variations of the electrical load, which reduce the lifetime of any energy

---

* Corresponding author at: Laboratoire d'Energétique Industrielle (LENI), Institut de Génie Mécanique, Ecole Polytechnique Fédérale de Lausanne, 1015 Lausanne, Switzerland. Tel.: +41 21 693 35 05; fax: +41 21 693 35 02.
E-mail address: arata.nakajo@epfl.ch (A. Nakajo).

0272-8842/$36.00 © 2012 Elsevier Ltd and Techna Group S.r.l. All rights reserved.
doi:10.1016/j.ceramint.2012.01.043

Nomenclature

Latin letters

b_E	constant
b_G	constant
b_σ	constant
d_g	particle diameter (m)
d^{crp}	creep particle exponent
D	diameter (m)
D^e	diffusion coefficient ($m^2\ s^{-1}$)
E	Young modulus (Pa)
E_a	activation energy ($J\ mol^{-1}$)
G	shear modulus (Pa)
h	thickness (m)
k_o	kinetic constant
m	Weibull modulus
m^{crp}	creep stress exponent
n	porosity
N	mechanical load (N)
R	universal gas constant 8.314 ($J\ mol^{-1}\ K^{-1}$)
T	temperature (K)
$\mathcal{V}_r$	reference volume (m^3)

Greek letters

α^{th}	coefficient of thermal expansion (K^{-1})
ϵ	strain
ϕ	scalar field variable
ν	Poisson's ratio
ρ	density ($kg\ m^{-3}$)
σ	stress (Pa)
σ_o	characteristic stress (Pa)
σ_u	threshold stress (Pa)

Indices

o	initial, dense state
cr	critical or failure
eq	equivalent
lr	loading ring
sp	sample
sr	supporting ring
th	thermal
RT	room temperature, 298 (K)

Superscripts

th	thermal
crp	creep
*	foam

Acronyms

BOR	ball-on-ring
CTE	coefficient of thermal expansion
GDC	gadolinia-doped ceria
LSM	lanthanum strontium manganite
LSCF	lanthanum strontium cobaltite ferrite
Ni–YSZ	nickel YSZ anode in reduced state
NiO–YSZ	nickel YSZ anode in oxidised state
ROR	ring-on-ring
SRU	single repeating unit
TBC	thermal barrier coating
XRD	X-rays diffraction
YDC	yttria-doped ceria
YSZ	yttria-stabilised zirconia
4PB	4-point bending

conversion device. The aggressive environment during constant output electrical power mode already entails detrimental alterations of the materials and interfaces. Coarsening of the microstructure [4–9], localised modifications of the composition of the materials close to the interfaces [10–12], development of insulating phases, such as lanthanum (LZO) or strontium zirconates (SZO) [13–15] or phase transformations [16,17] are commonly reported during aging, under polarisation or not. These phenomena can affect the mechanical behaviour of the cell layers, hence the ability of the cell to resist thermal cycling and/or electrical demand following.

Stresses in a cell embedded in a stack originate from different phenomena. Residual stresses build up after the sintering phase of the manufacturing process due to the mismatch between the coefficients of thermal expansion (CTE) of the materials of the cell. Stresses in the cell then arise from mechanical load due to the stacking and the joining with the components of the SRU frame by a glass sealant or compressive gaskets. The reduction of the nickel oxide in the anode takes place when fuel is fed for the first time, which ensures a suitable electrical conductivity and electrochemical activity. This last manufacturing step results in an increase in porosity, hence induces a change in mechanical properties and a shrinkage of the anode. During operation, the uneven temperature distribution causes additional stresses in the cell.

The stress state in the different layers of anode-supported cells follows typical patterns, depending on the range of possible variations of the CTE of the materials, which can be controlled to some extent by varying their composition. The anode support withstands tensile stress, while compressive stress shields the thin electrolyte, if their magnitude is properly controlled [18]. The use of separate or graded functional electrodes [19] and anode backside compensating layers to limit the cell curvature and to facilitate the assembly [20] does not modify this trend. The situation is less well defined in the cathode and possible compatibility layers. The two most widely used cathode materials, composite lanthanum strontium manganite and yttria-stabilised zirconia (LSM–YSZ) and single solid phase lanthanum strontium cobaltite ferrite (LSCF), have very different CTEs. LSM–YSZ can be subjected to either compressive or tensile stress, depending on the materials and temperature [21,22]. In the case of LSCF cathode, a compatibility layer made of gadolinia (GDC) or yttria-doped ceria (YDC) is required to prevent undesirable reactions at the interface between the cathode and the electrolyte [23,24]. Their CTE matches that of the anode; hence stress can possibly turn from tensile to compressive, or vice versa, depending on the anode state, temperature or cell thermal-history [25]. Since LSCF has usually the highest coefficient of thermal expansion among all layers, biaxial tensile stress is foreseen [22].

Besides support cracking, the failure modes in the thin functional electrodes, electrolyte, compatibility and collecting layers differ, whether the stress state is compressive or tensile. For instance, buckling-driven delamination can result from the former case, while the latter might induce cracking, channelling, spalling or delamination [26]. Different modelling approaches, such as fracture or damage mechanics or combinations of them, have to be used, depending on the issues to tackle [27]. The theory of continuum mechanics enables the structural analysis of the cell at the SRU scale. Further simplifications assume isotropy and linear elastic behaviour. The ceramic materials of the cell were found to comply well with these assumptions under SOFC conditions [28,29], though more complex behaviour such as low-temperature plasticity has been observed for some materials subjected to particular treatments [30–32]. The elastic properties and CTEs are first needed for the calculation of the stress distribution in the layers of the cell during operation. The knowledge of their dependences on temperature and upon aging and/or cycling provides first insights into possible degradation mechanisms. Other required data is the shrinkage strain in the anode due to the reduction procedure. A further step consists in including creep of the ceramic SOFC materials. The local and non-uniform irreversible deformation generated by creep relieve stresses under constant operating conditions. It decreases the shielding compressive stress in the electrolyte, which can affect the redox tolerance of the cell. It can also induce additional stresses and their redistribution during a variation of the operating conditions or a thermal cycle [25].

The knowledge of the stress field is a first step towards the analysis of the risks of failure of ceramic materials, such as provided by the Weibull theory [33]. However, more fundamental studies of the failure modes at smaller scales require the knowledge of fracture toughness of the bulk or interfaces, under different and mixed modes of loading, the measurement of which can be delicate.

SOFCs are comprised of composite materials, typically embedding ion and electron-conducting materials, to increase the number of electrochemically active sites in the electrodes. Their development can therefore benefit from the efforts to establish formal relationships between the microstructure of composite materials and their effective mechanical properties [34,35]. Qualitative analyses have been performed for SOFC materials, assuming either one constituent, or a combination of the constituents control the averaged properties of the composite material, e.g. CTE [36], Young's modulus [37] and creep behaviour [38,39].

The knowledge of the mechanical properties of SOFC materials is required to mitigate the foregoing issues. Though this topic has received growing interest in the past ten years, the data remains scarce for some materials and additional efforts are required. The present work seeks to compile available data on the mechanical properties of materials used in SOFCs. Sensitivity analyses of the effects of the disparities among the data compiled here on the stress distribution and the failure mechanisms in anode-supported SOFC is provided in Ref. [22]. Emphasis is placed on the properties required by the current approaches for structural analysis of intermediate-temperature, anode-supported SOFC SRU/stack, i.e. coefficients of thermal expansion, Young's modulus, Poisson's ratio, Weibull parameters and additional measurements of the anode reduction strains. Hence, fracture toughness of materials or interfaces is not reported here, despite its importance for other modelling approaches. Data on the fracture toughness of SOFC materials can be found in, e.g. Refs. [40–43]. The evolution of the properties during aging or cycling is the subject of current research and is included when available. Besides the data compiled from the literature, we include measurements of our Ni(O)–YSZ anode material: coefficient of thermal expansion in oxidised and reduced state, Young's modulus and strength, both at room temperature (oxidised and reduced state) and 1073 K (oxidised state).

2. Experimental

The tested anode composition is 55 wt.% of nickel oxide (NiO) powder (J.T.Baker), 22.50 wt.% of 3YSZ (Mel ox 3YUL) and 22.50 wt.% of 8YSZ (Mel ox 8YF) from MelChemical.The powder mixtures were homogenised with Duramax B1000 as a binder. It is referred as a1.

The samples for the determination of the Young modulus and CTE were prepared by dry pressing (PW 20, Paul-Otto Weber GmbH, Germany), with a pressure of 100 MPa, followed by sintering at 1673 K for 4 h with a heating and cooling rate of 3 K min^{-1} (HT 1750-6, Nabertherm, Germany). The specimens for fracture tests were discs produced by uniaxial pressing, followed by sintering at 1658 K for 4 h.

The CTE [44] of the anode materials was measured on a dilatometer (Bähr DIL 802L) with a SiC furnace, and alumina support and push road. The samples were bars of the size 5 mm × 5 mm × 25 mm. A type S thermocouple was applied on the sample for the measurement of the temperature. A calibration was previously done with a sapphire crystal against alumina. CTE measurements were carried out between room temperature and 1150 K, with a constant heating and cooling rate of 5 K min^{-1}.

The Young's modulus of the anode material was determined mechanically in 4-point bending on a test jig made of alumina oxide with loading rollers out of silicon carbide. The jig had a 40-mm support span and a 20-mm load span. The samples, in the form of bars, had a width between 4.25 and 4.65 mm, a height between 2.85 and 3.20 mm, and a length of approximately 45 mm. The test jig used had an integrated 3-point deflection measurement system where the outer measurements rods were located directly below the inner rollers. The test setup is shown schematically in Fig. 1 (bottom) and together with the oven in Fig. 1 (top). The measurements were performed in accordance to standard EN 843-2 [45] in air at room temperature, 1023 K and 1123 K. Hence reduced samples were only tested at room temperature. The samples for tests at

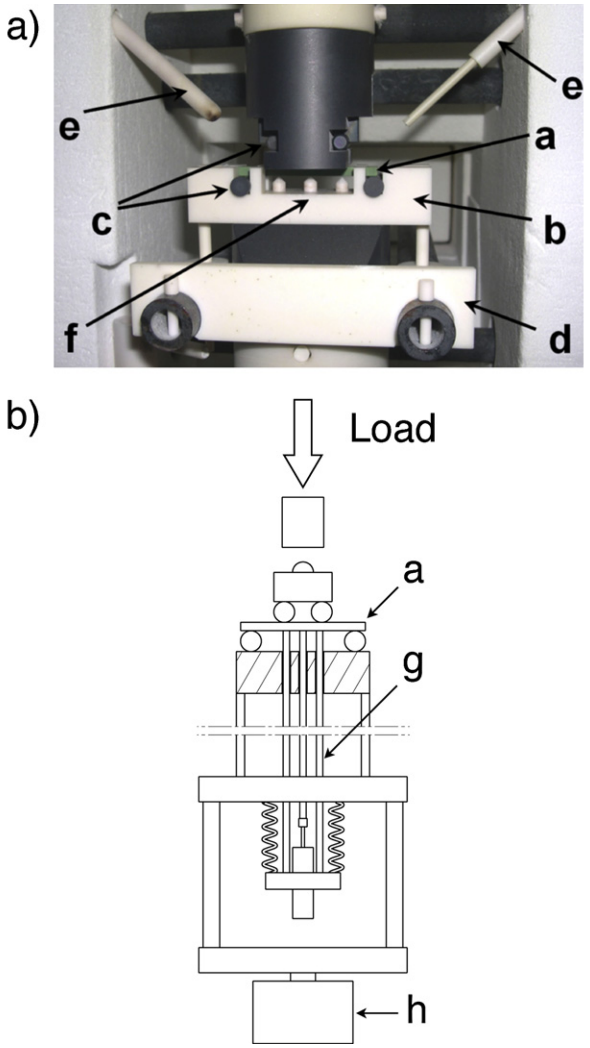

Fig. 1. Schematic view of 4-point test rig used for in-house measurements of the Young's modulus of Ni–YSZ and NiO–YSZ anodes (bottom) and picture of the test rig inserted into high temperature oven (top): (a) sample, (b) test jig (alumina oxide), (c) rollers (silicon carbide), (d) transport system, (e) thermocouples, (f) deflection measurement rods, (g) 3-point deflection measurement system, (h) load cell.

elevated temperatures were placed on the jig and inserted into the oven by a transport system over a time period of about 10 min resulting in heating rates between 75 K min^{-1} and 85 K min^{-1}. Before testing the samples were equilibrated for 10 minutes. To apply the load a universal test machine was used with a 2-kN load cell and cross-head displacement speed of 0.6 mm min^{-1}. The Young's moduli were calculated as the slope of the stress vs. deflection curve recorded during the 4-point bending tests. Five loading/unloading cycles per sample were performed for each value to be determined. The corresponding Young's moduli were computed in the interval comprised between 15–30% and 90% of the maximum applied load.

The experimental data needed to analyse the strength of the cermet by Weibull statistics was deduced from ring-on-ring bending tests in air, at room temperature and either room temperature or 1073 K for specimens in reduced, respectively oxidized state. The samples were discs with a diameter of 36 mm and a height of approximately 0.5 mm. Batches of 30 samples were tested for each condition. The test apparatus depicted in Fig. 2 has a load ring diameter of 12.5 mm and a support ring diameter of 25 mm. The slightly curved rim of the sample was placed cup-like towards the loading ring. The load was applied by a universal test machine with a load cell of 2 kN, at a cross-head displacement speed of 1.2 mm min^{-1} until fracture. The compliance of the setup was estimated at different temperatures with a 6 mm thick SiC sample to correct recorded load vs. displacement curves.

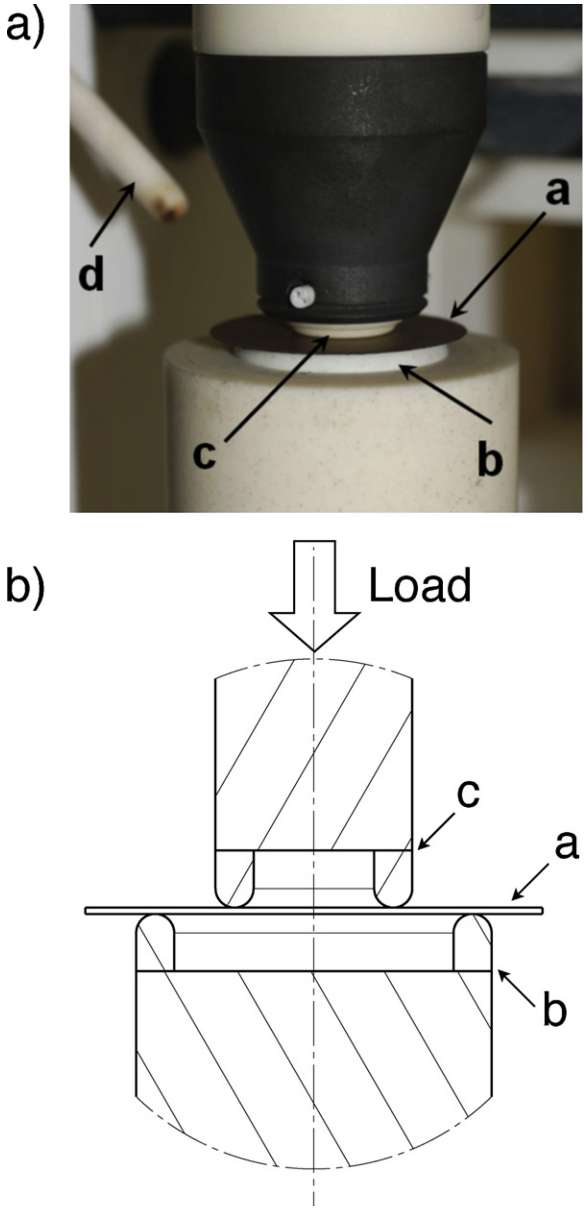

Fig. 2. Schematic view of ring-on-ring test rig (bottom) and picture of the test rig inserted into high temperature oven (top): (a) sample, (b) support ring (alumina oxide), (c) load ring (alumina oxide), (d) thermocouple.

3. Data compilation approach

3.1. Thermal and isothermal expansion

The CTEs of SOFC materials are available for a broad variety of compositions in different atmospheres. The CTE relates to key properties for SOFC application, such as oxygen non-stoichiometry, electronic and ionic conductivities and ion transport [46,47]. The thermal expansion observed during such measurements possibly contains a chemical contribution, depending on the environment during the measurement. Critical stresses and significant ensuing deformations in the SRU can arise from chemical (isothermal) expansions, when materials such as GDC or lanthanum chromite [48] are simultaneously subjected to reducing and oxidising atmospheres on different faces. The stress in standalone GDC electrolytes turns from compressive, initially induced by the residual stress, to tensile stress at some locations in operation, the magnitude of which is critical for the integrity of the layer [49–51]. In intermediate-temperature, anode-supported SOFC, GDC is used as a compatibility interlayer to prevent the development of insulating phases between the 8YSZ electrolyte and the LSCF cathode. The oxygen gradient to which it is subjected during normal operation, is therefore limited to a range where these effects can be neglected for the structural analysis at the SRU scale. Isothermal shrinkage occurs at least once in a SOFC stack, during the reduction of the anode. Defective SRU components or auxiliary devices or cracking of the electrolyte can induce anode redox cycling [52]. Information on chemical expansion is not reported here, with the exception of the dimensional changes of the anode induced by its initial reduction, due to the previously mentioned assumptions and the framework of the present study. Refs. [53,49,54,50,55,51,48] are a starting point to collect data to include in structural analysis chemical expansion during operation.

Most of the data on the CTEs consists of values for a single temperature difference, e.g. room temperature to 1273 K. In comparison, few temperature-dependent or differential values are readily available. Such values are required for a comprehensive study of the stresses in the cells. The thermal expansions between the reference state and those of interest, i.e. zero-stress and the temperature of operation, anode reduction, heat treatment of the glass sealant and room temperatures at least, have to be known. Here, temperature-dependent CTEs were computed from plots of expansion versus temperature taken from the literature.

The implementation of CTE differs depending on the modelling platform. Thermal expansion is computed in ABAQUS [56] from a temperature-dependent CTE, which expresses the total thermal expansion from a reference temperature, such as room temperature.

$$\epsilon^{th} = \alpha^{th}(T,\phi)\cdot(T-T_{RT}) - \alpha^{th}(T_o,\phi_o)\cdot(T_o-T_{RT}) \qquad (1)$$

The relation assumes that no strain exists even in the case the reference temperature does not equal the initial temperature. The data presented in this work is in the foregoing form for a reference temperature of 298 K. Simple adaptation might be required for use in other commercial finite-element tools. Shrinkage of the anode ensuing reduction or thermal cycling and isothermal expansion of stand alone GDC electrolyte can be implemented in finite-element tools either by conversion into thermal expansion or by build-in (swelling in ABAQUS) user subroutines.

3.2. Elastic properties

Different procedures exist for the measurement of the elastic properties. An evaluation of four different techniques is provided in Ref. [57]. The most common is the impulse excitation technique.

The Young's and shear moduli strongly depend on the porosity. Several relations applicable to homogenous materials with low porosity are available from the literature [40,58] and provide good predictions, even for either fully or partially reduced anode materials [59]. These relations can be used during the initial stages of the development of the cells, to identify trends when balancing electrochemical with structural considerations. This is of particular interest for the anode, as the microstructure, especially porosity, drastically changes after reduction. Parameters are provided for the two-parameter exponential, linear or non-linear relations, which are empirical, and the composite sphere model (CSM) [58,60]:

$$E = E_o\cdot\exp(-b_E n), \quad G = G_o\cdot\exp(-b_G n) \qquad (2)$$

$$E = E_o(1-b_E n), \quad G = G_o(1-b_G n) \qquad (3)$$

$$E = E_o\left(1-\frac{b_E n}{1+(b_E-1)n}\right), \quad G = G_o\left(1-\frac{b_G n}{1+(b_G-1)n}\right) \qquad (4)$$

$$E = E_o\frac{(1-n)^2}{1+b_E n}, \quad G = G_o\frac{(1-n)^2}{1+b_G n} \qquad (5)$$

The Poisson's ratio, when not readily provided in the sources, is computed assuming an homogeneous, linear isotropic material:

$$E = 2G(1+\nu) \qquad (6)$$

3.3. Strength

The strength of SOFC ceramic materials is not an intrinsic property, but strongly depends on the flaws and defects, that result from the manufacturing process and act as stress concentrators. Their failure stress is statistically distributed as a function of the flaw size distribution and depends on the size of the component. The Weibull analysis [33] is based on the weakest-link model, with an infinite number of links, the weakest one controlling the strength. The classical two-parameter version is valid for one defect population. It assumes a uniform stress distribution and a negligible size of the inhomogeneities, consequently size of the representative elementary volume, compared with that of the component.

Here, the representative elementary volume is the smallest volume whose failure provokes the failure of the whole structure. The two parameters are the Weibull modulus m and characteristic strength σ_o, which are respectively a measure of the width of the distribution and the stress at a probability of failure of 63%. If the representative elementary volume size is not negligible relative to that of the component, the weakest-link model has to be adapted for a chain with a finite number of links. The two-parameter Weibull distribution yields conservative predictions and is commonly used to analyse the results of strength measurements of SOFC materials.

The preferred test method is the ring-on-ring arrangement which generates a biaxial stress field and tests a larger volume [61]. As cracking is normally initiated inside the zone delimited by the smaller loading ring, this technique is relatively insensitive to the quality of the edges of the specimens. A large number of samples allow a reduction of the confidence interval, hence better reliability of the measurements, at the cost of increased experimental efforts. The formula for the calculation of the failure stress for small deformation is [62]:

$$\sigma_{cr} = \frac{3N_{cr}}{2\pi h_{sp}^2}\left((1-\nu)\frac{D_{sr}^2 - D_{lr}^2}{2D_{sp}^2} + (1+\nu)\ln\frac{D_{sr}}{D_{lr}}\right) \quad (7)$$

In the case the maximum deflection at failure load exceeds 1/2 h [63], as is likely for thin samples, Eq. (7) is not valid anymore. Finite-element correction for geometrical non-linearity must be applied to avoid any overestimation of the strength. The stress is no longer uniform under the area of the loading ring in the case of large displacement and presents a maximum at the tensile face, opposite to the loading ring [64]. This correction is implemented in an automatic manner in the post-processing of our experimental ring-on-ring strength test data. The samples are meshed with axisymmetric, second-order reduced-integration elements CAX8R in ABAQUS [56], while the application of the load is implemented as concentrated forces. Preliminary tests showed that the discrepancy in the results between this simplified approach and simulations considering frictionless contact between the sample and the rings remains negligible in the conditions treated here. A finite-element simulation is performed for each sample, characterised by a distinct thickness and mechanical load at failure, whereas uniform elastic properties are assumed for samples from a same batch. The present work uses the Young's moduli measured by the 4-point bend tests. The results of the simulations are then processed by MATLAB [65] built-in functions to compute the maximum likelihood estimates of the parameters, i.e. the characteristic strength and Weibull modulus along with the confidence intervals for a two-parameter Weibull analysis. In all cases, the reference volume is computed in accordance with the ASTM-C1499 norm [62]:

$$\mathcal{V}_r \approx \frac{\pi}{2}D_{lr}^2\left[\frac{h_{sp}}{2(m+1)}\right]\left[1 + \frac{44(1+\nu)}{3(1+m)}\frac{(5+m)}{(2+m)}\left(\frac{D_{sr}-D_{lr}}{D_{sr}D_{sp}}\right)^2 \times\left(\frac{2D_{sp}^2(1+\nu) + (D_{sr}-D_{lr})^2(1-\nu)}{(3+\nu)(1+3\nu)}\right)\right] \quad (8)$$

which induces an error of 5%, for $m \geq 5$ and $D_{sr}/D_{lr} = 0.2$. This procedure is not fully consistent, but is adopted, since the observed correction for large displacement is small for the approximatively 500 μm thick samples used for the in-house measurements. Either surface or volume has to be considered, depending on the strength controlling defects. A systematic use of the former is not necessarily physically rigorous, but conservative in the case the actual stack component is thicker than the test sample.

3.4. Creep behaviour

Creep occurs when the material is constantly loaded at a temperature near one half of its melting point. This slow and continuous deformation can be classified into three main categories, depending on the mechanism: diffusion, viscous and dislocation creep. Difficulties arise from the temperature-dependence and possible overlapping or changes in the dominant mechanism. In the case of SOFC materials, most of the few existing data comes from measurements at temperatures significantly higher than those encountered during normal operation of intermediate-temperature SOFC stacks. The needed extrapolation can lead to seriously misleading predictions.

The creep behaviour of a material may differ, when subjected to tensile and compressive stress [66]. Creep parameter extraction from bend tests data is more complicated, owing to the stress gradient in the sample [67,68]. The data reported in the present study is restricted to steady-state (secondary) creep and assumes similar material behaviour in tension and traction. This simplification is found in other research domains [69]. Diffusion creep can be modelled by a general expression:

$$\dot{\epsilon}_{eq}^{crp} = \frac{\tilde{k}_o^{crp} D^e}{T}\frac{\sigma_{eq}^{m^{crp}}}{d_g^{d^{crp}}} \quad (9)$$

Here, σ_{eq} is an equivalent stress such as the von Mises one and $\dot{\epsilon}_{eq}^{crp} = \sqrt{2/3\dot{\epsilon}_{ij}^{crp}\dot{\epsilon}_{ij}^{crp}}$. The values of the stress and grain size exponents differ depending on the operating mechanism. For instance, Nabarro-Herring creep yields $m^{crp} = 1$ and $d^{crp} = 2$, while $d^{crp} = 3$ for Coble creep [70]. The relation can be conviently simplified and recasted for implementation in finite-element software, as the grain size dependence is not explicitely required:

$$\dot{\epsilon}_{eq}^{crp} = k_o^{crp}\exp\left(-\frac{E_a^{crp}}{RT}\right)\sigma_{eq}^{m^{crp}} \quad (10)$$

The temperature dependence mainly arises from the diffusion coefficient of species controlling the creep rate. Eq. (10) is used for the analysis of the compiled data. The determination of the values reported in the present study proceeds by first using activation energies and stress exponents provided by the sources corresponding to the closest conditions to those in a stack during operation, in terms of temperature, stress range and deformation. k_o^{crp} is then deduced from available figures. It therefore does not include a combined estimation of the three parameters, k_o^{crp}, E_a^{crp} and m^{crp}. As this compilation is meant for preliminary studies of the effects of creep on the structural issues in SRUs, data from measurements at the lowest temperatures is preferentially reported.

Data on dense materials can be corrected to consider the porous nature of the electrode and gas diffusion layers. Besides the correction for an averaged effective stress, research on cellular materials yielded relations based on considerations on the different possible deformation modes of the struts. Their validity is tested against finite-element simulations of the creep deformation at the representative elementary volume scale [69]. This approach, while coarse, is believed to be adequate for preliminary studies, because of the actual uncertainties on the creep behaviour of SOFC materials. The two most common relations are based on different assumptions on the deformation of the struts. In Eq. (11) [71] (Eq. (12) [72]) the vertical (horizontal) stays rigid, while the horizontal (vertical) is deformed by bending (compressive) creep.

$$\dot{\epsilon}_{eq}^{crp} = k_o^{crp}\exp\left(-\frac{E_a^{crp}}{RT}\right)\frac{0.6}{m^{crp}+2}\left(\frac{1.7(2m^{crp}+1)}{m^{crp}}\right)^{m^{crp}} \times \sigma_{eq}^{m^{crp}}\left(\frac{\rho^*}{\rho_o}\right)^{-(3m^{crp}+1)/2} \qquad (11)$$

$$\dot{\epsilon}_{eq}^{crp} = k_o^{crp}\exp\left(-\frac{E_a^{crp}}{RT}\right)\left(\frac{1}{3}\frac{\rho^*}{\rho_o}\right)^{-m^{crp}}\sigma_{eq}^{m^{crp}} \qquad (12)$$

The creep strain rates predicted by these two relations significantly differ. Eq. (11), which certainly has a more solid physical meaning, yields higher values than Eq. (12). However, since this study places the emphasis on reproducing the collected experimental data, either relation is selected here to satisfy agreement with experiments.

4. Compiled data

4.1. Electrolytes and compatibility layers

8 mol% YSZ (8YSZ) has received most of the attention as SOFC electrolyte material due to its superior thermal and electrical properties. Its choice is somewhat compromised when it comes to strength or long-term stability of the ionic conductivity [73–76]. The decrease of the thickness of the electrolyte is one reason for the higher performance of anode-supported cell, as compared with electrolyte-supported cells. The typical thicknesses range from 4 μm to 15 μm in anode supported cells and 100 μm to 300 μm in electrolyte supported cells. A dense material is required to ensure the separation of the fuel and air compartments.

GDC has been proposed as an electrolyte for low-temperature SOFC or compatibility layers in LSCF cathode-based cells, though a presence of small electronic conductivity and vulnerability towards isothermal expansion are two major drawbacks for the former application. In the present study, GDC and YDC are considered as compatibility layers, to prevent reaction between the 8YSZ electrolyte and the LSCF cathode. Dense compatibility layers could not be produced at the beginning of their development. Their porosity affected their protective effect, but this issue has since been solved [23,24].

Fig. 3 depicts the compiled data on the CTE of these materials. The CTE of ceria-based materials is significantly higher than that of YSZ, whereas the typical range of variation between room temperature and usual operating or sintering temperatures is approximately 0.8×10^{-6} to 1.2×10^{-6} K^{-1}. Mori et al. [36] did not find any significant influence of the oxygen partial pressure on the CTE of 8YSZ. This is not the case of GDC (see discussion on isothermal expansion in Section 3.1). All measurements presented in Fig. 3 were performed in air.

The CTE of both materials exhibits temperature dependence. SRU typically have to withstand spatial temperature differences in the range of 100 K, e.g. [77,78,21,79]. The corresponding variations of the CTE in one data set are spread over approximately 0.2×10^{-6} K^{-1}, which can lead to imprecision in the calculation of the stress field [22]. The increase of the CTE of YSZ with temperature is attributed to the volume expansion associated to the formation of point defects [36]. Hayashi et al. [47,80] tried to elude the effect of the content of gadolium and yttria on the CTE of GDC and YSZ, respectively, and observed opposite trends for the two materials. In GDC, higher CTEs are reported for increased Gd content, as a result of the increase of the oxygen vacancy concentration and ensuing weakening of the binding energy [47]. This does not hold for the yttria content of YSZ. Hayashi et al. [80] attributed the decrease in CTE for higher yttria

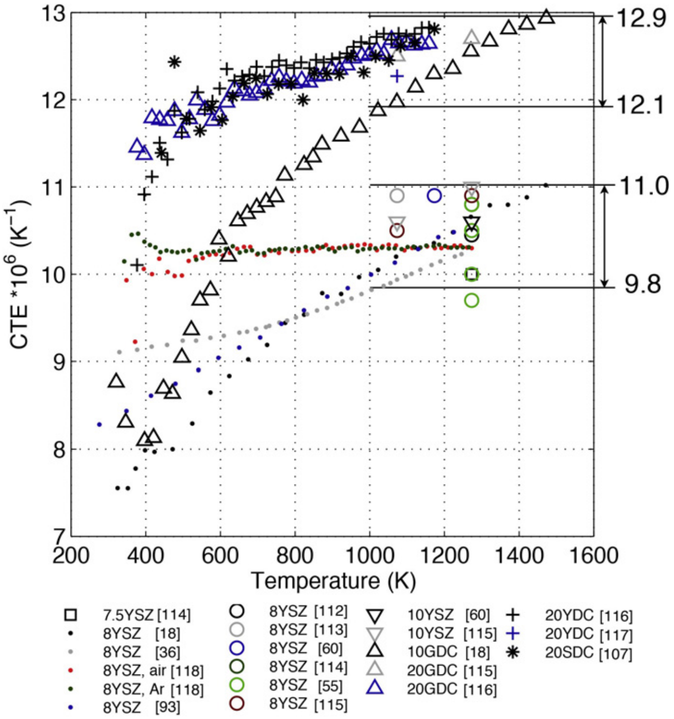

Fig. 3. Temperature dependent CTEs of YSZ, YDC and GDC [18,36,93,112–114,55,60,115,116,107,117,118]. (For interpretation of colour in the artwork the reader is referred to the web version of the article.)

content to the variation of the bulk modulus, as this parameter, which increases with the yttria content, has a strong influence in their theoretical model. This is not clearly seen in Fig. 3, and has not been confirmed by all studies [81].

The reported stress–strain curves of YSZ are linear over the investigated temperature range (not depicted) [28,82]. Temperature-dependent and single temperature measurements of the Young's moduli of YSZ and GDC materials are depicted in Fig. 4. The values are comparable for both materials. The curves corresponding to different compositions and measurements exhibit similarities for YSZ. After an initial decrease up to approximately 680–830 K, the Young modulus follows a plateau or a mild increase and then decreases around 1473 K, when data is available. The first feature matches the temperature range where internal friction experiments reveal one or two peaks, for 3YSZ and higher yttria contents [83,84]. Possible causes of this mechanical loss are the reorientation jumps of $V_o^{\cdot\cdot} - Y_{Zr}$ pairs and the relaxation of the oxygen vacancies within a cluster of two or more yttrium ions [84,85]. The effect of oxygen partial pressure on the Young's modulus of 8YSZ is limited [86]. A decrease in the range of 15% is observed, when varying the oxygen partial pressure from that of air to 10^{-22} [54]. For 10GDC, the decrease is of approximately 20% under the same conditions, but GDC compatibility layers in anode-supported cells with LSCF cathode are not subjected to such oxygen partial pressure gradients. The parameters for the different correlations between porosity and Young modulus are listed in Table 1. Eqs. (4) and (5) provide equally good

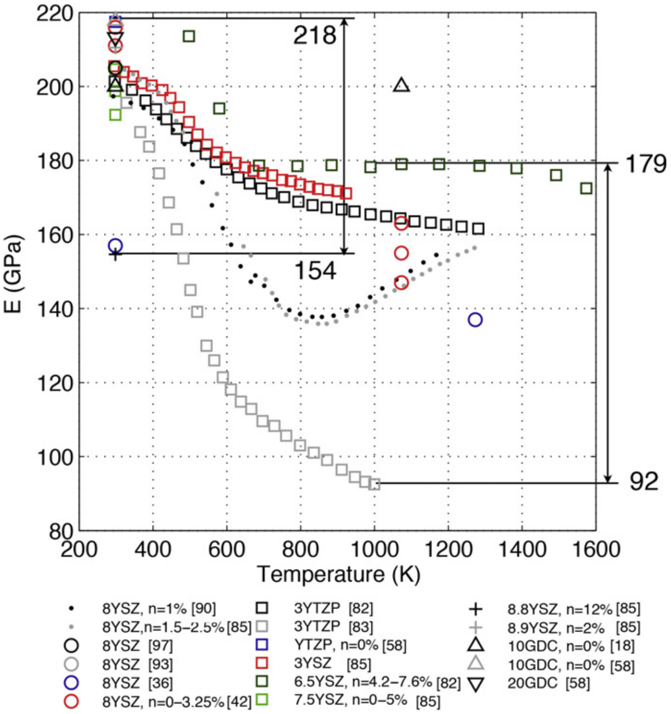

Fig. 4. Temperature dependent Young modulus of YSZ and GDC [18,36,58,42,93,82,83,85,90,97]. (For interpretation of colour in the artwork the reader is referred to the web version of the article.)

Table 1
Parameters for the calculation of porosity-dependent elastic properties. Values corresponding to the standard deviation are provided inside the brackets, when available in the original source.

Material	Model	E_o (GPa)	b_E	G_o (GPa)	b_G	
NiO–YSZ (75 mol% NiO)	Exponential (Eq. (2))	210.8 [209.4; 212.2]	2.70 [2.66; 2.74]	80.4 [79.9; 80.9]	2.60 [2.56; 2.64]	[40]
NiO–YSZ (75 mol% NiO)	CSM (Eq. (5))	209.5 [208.1; 210.9]	0.46 [0.51; 0.41]	79.4 [78.8; 80.0]	0.33 [0.28; 0.38]	[40]
NiO–YSZ (50–55 wt.% NiO)	Linear (Eq. (3))	206.9	2.12	–	–	[37]
NiO–YSZ (75 mol% NiO)	Exponential (Eq. (2))	207.1	2.48	78.0	2.38	[58]
NiO–YSZ (75 mol% NiO)	Non-linear (Eq. (4))	207.2	2.55	78.0	2.42	[58]
NiO–YSZ (75 mol% NiO)	Linear (Eq. (3))	205.5	2.10	77.5	2.03	[58]
NiO–YSZ (75 mol% NiO)	CSM (Eq. (5))	218.8	0.93	80.6	0.77	[58]
Ni–YSZ (75 mol% NiO)	Exponential (Eq. (2))	212.1 [210.8; 213.4]	3.16 [3.13; 3.19]	79.5 [78.9; 80.1]	2.95 [2.92; 2.98]	[40]
Ni–YSZ (75 mol% NiO)	CSM (Eq. (5))	211.4 [210.5; 212.3]	0.79 [0.77; 0.81]	78.2 [77.8; 78.6]	0.53 [0.51; 0.55]	[40]
Ni–YSZ (50–55 wt.% NiO)	Linear (Eq. (3))	205.9	1.76	–	–	[37]
8YSZ	Exponential (Eq. (2))	220.3	−2.76	83.5	2.63	[58]
8YSZ	Non-linear (Eq. (4))	220.5	2.84	83.5	−2.69	[58]
8YSZ	Linear (Eq. (3))	219.5	−2.50	83.2	−2.39	[58]
8YSZ	CSM (Eq. (5))	223.9	1.04	84.7	0.93	[58]
3YTZP	Exponential (Eq. (2))	217.5	−3.01	81.5	2.91	[58]
3YTZP	Non-linear (Eq. (4))	218.9	3.23	81.5	−3.09	[58]
3YTZP	Linear (Eq. (3))	213.2	−2.48	80.0	−2.41	[58]
3YTZP	CSM (Eq. (5))	217.8	0.99	81.5	0.86	[58]
10GDC	Exponential (Eq. (2))	217.8	2.92	81.6	2.76	[58]
10GDC	Non-linear (Eq. (4))	218.1	3.01	81.7	2.83	[58]
10GDC	Linear (Eq. (3))	217.0	2.67	81.3	2.54	[58]
10GDC	CSM (Eq. (5))	218.5	1.00	81.9	0.88	[58]
20GDC	Exponential (Eq. (2))	213.3	2.64	79.9	2.47	[58]
20GDC	Non-linear (Eq. (4))	213.6	2.71	80.0	2.52	[58]
20GDC	Linear (Eq. (3))	212.2	2.39	79.6	2.25	[58]
20GDC	CSM (Eq. (5))	216.6	1.00	81.2	0.87	[58]

predictions for the tested electrolyte materials, the porosity of which ranged from approximately 0 to 10%[58]. The values of the Poisson's coefficients are summarised in Table 2.

Weibull parameters for YSZ and GDC materials are available from measurements at room and operating temperature in air. The data compiled in Table 3 complies to the assertment that 3YSZ is preferable to 8YSZ from a mechanical perspective. The Weibull modulus is usually lower than the threshold of 10 for technological ceramics. The effect of the oxygen partial pressure on the strength of 8YSZ and 10GDC matches that of the Young's modulus [54]. The strength of YSZ decreases with temperature increase, while the trend is opposite for GDC [60]. Lowrie et al. [87] observed different fracture behaviours, depending on the temperature. Whereas fracture initiated from defects very close to the surface of the sample at room temperature, the initiation site could not be always related to a defect at higher temperature. By increasing the temperature, the propagation mechanism concurrently changed from transgranular to mixed transgranular and intergranular for samples tested at 1273 K. As mentioned previously, the strength of SOFC materials is strongly affected by the manufacturing process. Atkinson et al. [18] noted an increase in apparent strength of 8YSZ/20GDC laminates compared with that of individually tested YSZ and GDC specimens. This improvement could be attributed to the reduction of the surface roughness thanks to the lamination process and shielding effect of the compressive stresses in the YSZ, when the testing arrangement induced an initiation of the fracture at the interface. Weibull parameters for YDC could not be found. The study of Ishida et al. [88] suggests values and a temperature dependence similar to those of GDC.

Information on the effects of cycling and aging on the foregoing properties is limited to the strength of 8YSZ. The cubic to tetragonal phase transformation is a possible reason for the observed decrease in the ionic conductivity of YSZ during aging, though the mechanisms have not yet been unambiguously

Table 2
Poisson's ratio of SOFC materials. Values corresponding to the standard deviation is provided inside the brackets, when available in the original source.

Material	n (%)	$T_{measure}$ (K)	ν[b]	
8YSZ	–	298	0.32	[93]
8YSZ	–	298	0.29	[36]
8YSZ	–	1273	0.29	[36]
Ni–8YSZ/8YSZ (75 mol% NiO)	40	298	0.12	[101]
Ni–8YSZ/8YSZ (75 mol% NiO)	39	298	0.05	[101]
Ni–8YSZ/8YSZ (75 mol% NiO)	36	298	0.29	[101]
Ni–8YSZ/8YSZ (75 mol% NiO)	35	298	0.23	[101]
Ni–8YSZ/8YSZ (75 mol% NiO)	27	298	0.29	[101]
Ni–8YSZ/8YSZ (75 mol% NiO)	27	298	0.28	[101]
Ni–8YSZ/8YSZ (75 mol% NiO)	40	298	0.29	[101]
Ni–8YSZ/8YSZ (75 mol% NiO)	40	298	0.32	[101]
Ni–8YSZ/8YSZ (75 mol% NiO)	40	298	0.30	[101]
Ni–8YSZ/8YSZ (75 mol% NiO)	40	298	0.31	[101]
Ni–8YSZ/8YSZ (75 mol% NiO)	34	298	0.31	[101]
Ni–8YSZ/8YSZ (75 mol% NiO)	34	298	0.31	[101]
Ni–8YSZ/8YSZ (75 mol% NiO)	35	298	0.34	[101]
Ni–8YSZ/8YSZ (75 mol% NiO)	35	298	0.29	[101]
Ni–8YSZ/8YSZ (75 mol% NiO)	27	298	0.29	[101]
Ni–8YSZ/8YSZ (75 mol% NiO)	26	298	0.29	[101]
Ni–8YSZ/8YSZ (75 mol% NiO)	26	298	0.30	[101]
Ni–8YSZ/8YSZ (75 mol% NiO)	27	298	0.30	[101]
NiO–8YSZ/8YSZ (70 mol% NiO), 0.6 mm	10	298	0.22	[98]
NiO–8YSZ/8YSZ (70 mol% NiO), 0.9 mm	10	298	−0.28	[98]
Ni–8YSZ/8YSZ (70 mol% NiO), 0.6 mm	35	298	0.12	[98]
Ni–8YSZ/8YSZ (70 mol% NiO), 0.9 mm	40	298	−0.25	[98]
NiO–3YSZ (50–55 wt.% NiO)	20[a]	298	0.39	[37]
Ni–3YSZ (50–55 wt.% NiO)	35[a]	298	0.39	[37]
$La_{0.2}Sr_{0.8}Co_{0.2}Fe_{0.8}O_3$	–	298	0.26 [0.23; 0.29]	[41]
$La_{0.4}Sr_{0.6}Co_{0.2}Fe_{0.8}O_3$	–	298	0.32 [0.30; 0.34]	[41]
$La_{0.6}Sr_{0.4}Co_{0.2}Fe_{0.8}O_3$	–	298	0.32 [0.31; 0.33]	[41]
$La_{0.8}Sr_{0.2}Co_{0.2}Fe_{0.8}O_3$	–	298	0.32 [0.316; 0.324]	[41]
$La_{0.8}Sr_{0.2}MnO_3$	29	298	0.28	[85]
$La_{0.8}Sr_{0.2}MnO_3$	12	298	0.34	[85]
$La_{0.8}Sr_{0.2}MnO_3$	9	298	0.35	[85]
$La_{0.8}Sr_{0.2}MnO_3$	4	298	0.36	[85]

[a] Estimated.

[b] Computed by Eq. (6), when not directly provided in the original source.

Table 3
Weibull parameters and strength of electrolyte materials. Values inside brackets refer to the 95% confidence interval.

Material	Aging (air)	T_{msrmt} (K)	n (%)	Method	σ_o/MOR (MPa)	m	Samples	$\mathcal{V}_r$ (mm^3)	
8 mol% YSZ	–	298	1.68	Tensile test	217	–	1	–	[28]
8 mol% YSZ	1273 K, 1000 h	298	1.68	Tensile test	293	–	1	–	[28]
10 mol% CGO	–	298	2–5	ROR	134	3.8	15	1.028	[60]
10 mol% CGO	–	1073	2–6	ROR	183	5.7	15	0.575	[60]
20 mol% CGO	–	298	2–6	ROR	148	6.0	10	0.561	[60]
8 mol% YSZ	–	298	1–7	ROR	232	5.7	10	0.535	[60]
8 mol% YSZ	–	1073	1–7	ROR	154	8.6	10	0.301	[60]
8 mol% YSZ	–	298	1–7	ROR	192	6.9	10	0.409	[60]
8 mol% YSZ	–	1073	1–7	ROR	131	5.6	10	0.547	[60]
3 mol% YTZP	–	298	5–10	ROR	423	3.5	10	1.006	[60]
3 mol% YTZP	–	1073	5–10	ROR	165	3.9	10	0.861	[60]
8 mol% YSZ	–	298	–	ROR	171	5.0	16	6.372	[61]
8 mol% YSZ	–	298	–	ROR	211	9.0	16	3.860	[61]
8 mol% YSZ	1223 K, 1300 h, 22 cycl.	298	–	ROR	211	6.36	16	5.731	[61]
7.7 mol% YSZ	–	298	–	ROR	332	5.1	15	0.512	[87]
7.7 mol% YSZ	–	1223	–	ROR	256	4.5	20	0.613	[87]
7.7 mol% YSZ	1123 K, 1000 h	298	–	ROR	353	5.2	20	0.498	[87]
7 mol% YSZ	–	298	–	ROR	294	5.1	15	0.512	[87]
7 mol% YSZ	–	1123	–	ROR	205	7.3	14	0.309	[87]
3 mol% YSZ	–	298	–	ROR	1300 [1260; 1340]	8 [6; 10]	8[a]	0.010	[122]
3 mol% YSZ	–	1073	–	ROR	610 [590; 620]	10 [6; 14]	7[a]	0.010	[122]
3 mol% YSZ	–	298	–	ROR glued foil	600 [570; 630]	8.7 [6.7; 10.7]	11[a]	31.4[c]	[122]
10CGO (8YSZlaminated)	–	298	–	ROR	413	4.6	13	[b]	[18]
10CGO (8YSZlaminated)	–	1073	– –	ROR	394	7.0	13	[b]	[18]
8YSZ (8YSZlaminated)	–	298	–	ROR	216	7.4	13	[b]	[18]
8YSZ (8YSZlaminated)	–	1073	–	ROR	257	5.4	13	[b]	[18]
8 mol% YSZ	–	298	–	ROR	446	6.7	34	0.350	[64]
8 mol% YSZ	–	1173	–	ROR	282	8.0	20	0.273	[64]

[a] From Weibull plot.

[b] Eq. (8) not applicable.

[c] Volume delimited by the supporting ring.

clarified [17,73–75,89]. At a first appraisal, a concurrent increase in the strength is expected in the case this phase transformation effectively occurs and affects the ionic conductivity, as observed by Kondoh et al.[28] by comparing the tensile strength of nascent sample to that of samples aged in air at 1273 K for 1000 h. In contrast, other aging studies do not show any significant strength improvement in similar conditions [87,61]. These strength measurements on aged samples, together with aging conditions, are included in Table 3.

Data on bending creep of 8YSZ and 20YDC in a temperature range of 1223–1563 K and 1323–1398 K, respectively, is available in [87,90,91]. Table 4 lists the parameters determined from [87,91]. Fig. 5 depicts a comparison of the computed strain rates with the overall set of measurements, to check that the predicted strain rates lie within the proper orders of magnitude. The acceptable match between the activation energies of creep and diffusion of Zr cations (460 kJ mol^{-1}) and stress exponent close to 1 suggest that the creep deformation of 8YSZ is controlled by grain-boundary diffusion [87] at SOFC operating temperature. At higher temperature, bulk cation diffusion is likely responsible for creep [90]. The values of m^{crp}, d^{crp} and E_a^{crp} reported for 20YDC are in agreement with Nabarro-Herring creep [91].

4.2. Ni–YSZ anodes

Ni–YSZ cermets are preferred for SOFC anodes thanks to their good electrochemical and chemical activity. Their composite nature enables a spreading of the electrochemically active zone, by increasing the triple-phase boundary length

Table 4
Parameters for the estimation of creep strain rates in SOF cell materials.

Material	k_o^{crp} (MPa^m h^{-1})	E_a^{crp} (kJ mol^{-1})	m^{crp}	
8YSZ	1.836e+07	320	0.5	[87]
8YSZ	4.373e+07	370	1.0	[90]
Ni–YSZ (56 wt.% NiO)	3.714e−02	115	1.7	[68]
Ni–3YTZP (40 vol.% Ni)	1.040e+20	640	2.5	[39]
20YDC	6.768e+04	264	1.0	[91]
$La_{0.5}Sr_{0.5}Fe_{0.5}Co_{0.5}O_3$	5.551e+10	392	1.7	[111]

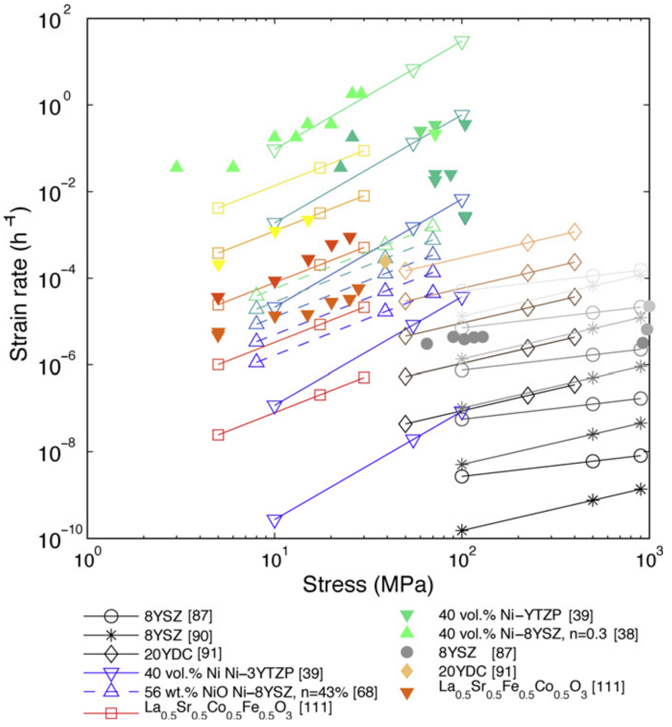

Fig. 5. Qualitative comparison of computed (lines) and experimental (filled markers) creep strain rates of SOF cell materials. The respective stress ranges correspond to those expected in SOFCs. [38,39,87,91,111,68,90]. The temperature range of 993–1373 K is depicted by colour variations: Ni–YSZ, blue to green, LSCF, red to yellow, YSZ, black to grey and YDC, black to brown. (For interpretation of colour in the artwork the reader is referred to the web version of the article.)

(TPBL) per electrode volume. Both electrode performance and structural stability require the percolation of the porous as well as the ionic and electronic-conducting phases. The final microstructure depends on the powder size distribution, the initial composition, the manufacturing route and the reduction procedure [37,92]. The anode support plays the key role in the structural integrity of the cell. Its porosity has to be tailored, depending on its thickness, e.g. 300–2000 μm, to enable the diffusion of reactants and products. This requirement differs from that of a high TPBL. Hence, a differentiation between the anode-supporting and anode-functional layers is found in state-of-the-art cells.

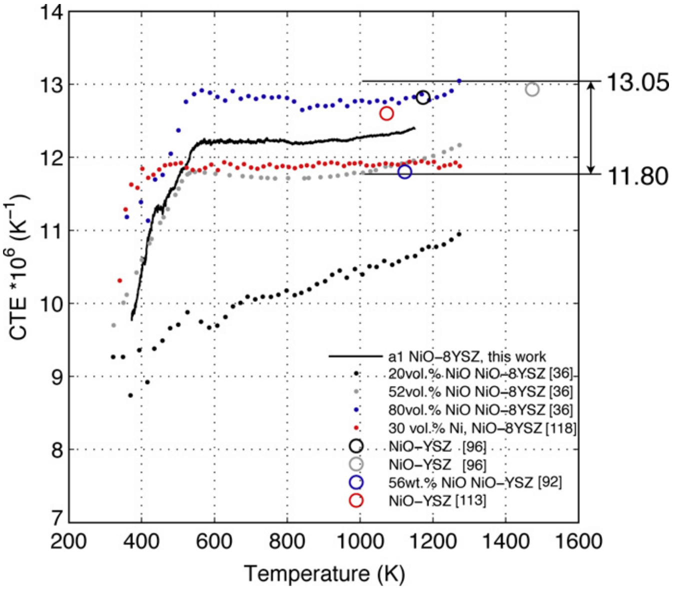

Fig. 6. Temperature dependent CTEs of the anode in oxidised state [36,92,113,118,96]. (For interpretation of colour in the artwork the reader is referred to the web version of the article.)

The CTEs of Ni–YSZ anodes is available for different compositions and states. Figs. 6 and 7 show the results of the literature survey, along with our measurements in oxidised and reduced states, respectively. The reported values of the CTE required for the calculation of thermal stresses at room temperature and operation temperature are comprised within 12.27×10^{-6} to $13 \times 10^{-6}\ \mathrm{K}^{-1}$ for oxidised and 11.2×10^{-6} to $13.3 \times 10^{-6}\ \mathrm{K}^{-1}$ for reduced state. Such large variations strongly affect the calculation of the stress field, which can turn from compressive to tensile in the cathode [22]. The CTE increases for higher NiO or Ni contents. An anomaly due to the antiferromagnetic to paramagnetic transition of NiO, and the ferromagnetic to paramagnetic transition of metallic Ni, which entails a change in the structure from rhombohedral to cubic structure in the case of NiO is seen in the differential coefficient of thermal expansion (not depicted). It is located around 530 K and 631 K for NiO and Ni, respectively [36,37,93].

Mori et al. [36] report a difference in the behaviour of NiO–YSZ and Ni–YSZ at the highest temperatures. A decrease of the differential CTE at temperature higher than 1173 K occurs for the latter materials, due to the significant plastic deformation of

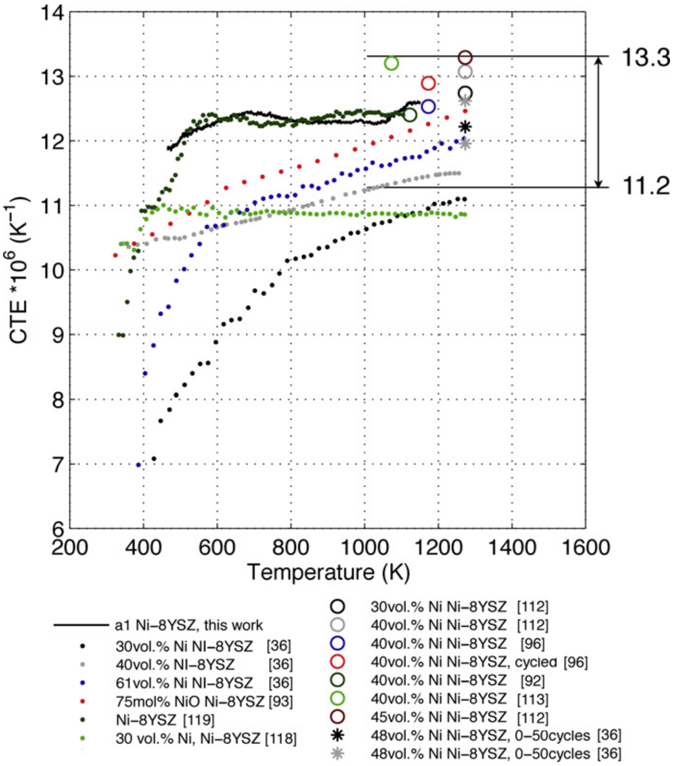

Fig. 7. Temperature dependent CTEs of the anode in reduced state [36,92,93,112,113,118,96,119]. (For interpretation of colour in the artwork the reader is referred to the web version of the article.)

Table 5
Collected data on reduction strain of the anode material.

Material	Reduction conditions	ϵ_r (%)	
Ni–3YSZ (50–55 wt.% NiO)	9% H_2/91% N_2, 1123 K	0.00e+00	[123]
Ni–3YSZ (50–55 wt.% NiO)	9% H_2/91% N_2, humid, 1123 K	−1.00e−02	[123]
Ni–3YSZ (50–55 wt.% NiO)	9% H_2/91% N_2, 1273 K	−2.00e−02	[123]
Ni–8YSZ (40 vol.% Ni)	9% H_2/91% N_2, 1123 K	−2.91e−01	[92]
Ni–8YSZ (40 vol.% Ni)	9% H_2/91% N_2, 1123 K	−5.40e−01	[92]
Ni–8YSZ (40 vol.% Ni)	9% H_2/91% N_2, 1123 K	−2.34e+00	[92]
Ni–8YSZ (40 vol.% Ni)	9% H_2/91% N_2, 1123 K	−6.33e−02	[92]
Ni–8YSZ (40 vol.% Ni)	9% H_2/91% N_2, 1123 K	−4.43e−01	[92]
Ni–3YSZ (50–55 wt.% NiO)	9% H_2/91% N_2, 1123 K	−9.60e−02	[94]
Ni–3YSZ (50–55 wt.% NiO)	9% H_2/91% N_2, 1123 K	−1.06e−01	[94]
Ni–3YSZ (50–55 wt.% NiO)	9% H_2/91% N_2, 1123 K	−2.00e−01	[94]
Ni–3YSZ (50–55 wt.% NiO)	9% H_2/91% N_2, 1123 K	−1.31e−01	[94]
Ni–3YSZ (50–55 wt.% NiO)	9% H_2/91% N_2, 1123 K	−1.68e−01	[94]
Ni–3YSZ (50–55 wt.% NiO)	9% H_2/91% N_2, 1123 K	−1.80e−01	[94]
Ni–3YSZ (50–55 wt.% NiO)	9% H_2/91% N_2, 1123 K	−3.01e−01	[94]
Ni–8YSZ (56 wt.% NiO)	10% H_2/90% N_2, 1173 K	−1.70e−02	[59]

the Ni particles as a result of its interaction with the YSZ backbone. This trend is not seen in all the measurements. This could be due to a difference in the microstructure of the samples, heating ramps (2–5 K min^{-1}) or a limitation of the experimental setup.

Data on the reduction strain is reported in studies of the redox behaviour of anode supports. This topic is not considered in the present survey. Table 5 only lists values for the initial reduction. As expected, considerable discrepancies exist among the measurements. The largest strain value of -2.34×10^{-2} exceeds the contribution of the typical pursued CTE mismatch between SOFC materials which lies between 10^{-3} and 10^{-2}. Grahl-Madsen et al. [92] used dilatometry to study the reduction behaviour of 40 vol.% Ni Ni–8YSZ anodes, processed by different routes. They observed a strong dependence of both overall reduction rates and final measured shrinkage, due to the different microstructures. The rate depends on the size of the NiO particles, while the shrinkage is mainly related to the strength of the 8YSZ backbone. Pihlatie et al. [94] used the same measurement technique on 50–55 wt.% NiO Ni–3YSZ specimens of different porosities, at different temperatures with or without humidity. The reduction strain depends on the reduction temperature, but also on the humidity of the feed gas. Almost no variation occurs at 1123 K, while a small value of 0.01% and 0.02% is measured at 1273 K and humid conditions at 1123 K, respectively. Malzbender et al. [95] and Sun et al. [96] derived values from the analysis of the curvature of the anode support. The behaviour differs, depending on the anode support arrangement, such as presence or not of a compatibility layer. Sun et al. [96] hence suggest that a significant amount of plastic deformation of the Ni phase occurs during reduction.

The reduction procedure entails an increase in porosity of the anode material, which is well predicted by the relation proposed by Radovic et al. [40]:

$$n_{\text{Ni-YSZ}} = 0.228 + 0.772 n_{\text{NiO-YSZ}} \tag{13}$$

Different recommendations on the choice of correlations (see Section 4.1) between porosity and elastic properties at room temperature emanate from the study on SOFC anodes. The exponential and CSM models properly fitted the experimental data of Radovic et al. [40], while Pihlatie et al. [37] investigated a larger range of porosities, up to 50%, and observed a linear dependence. Atkinson et al. [58] discarded the CSM model for their NiO–8YSZ samples, which formally applies to two-phase, rather than to three-phase materials, such as a porous Ni-based SOFC anode. Table 1 lists the values of the parameters.

Data on the temperature dependence of the Young's modulus of the common compositions of Ni–YSZ anodes remain scarce, but all reported trends are fairly similar [37,97,98]. Figs. 8 and 9 depict our measurements together with compiled data, with the exception of measurements of the porosity dependence at room

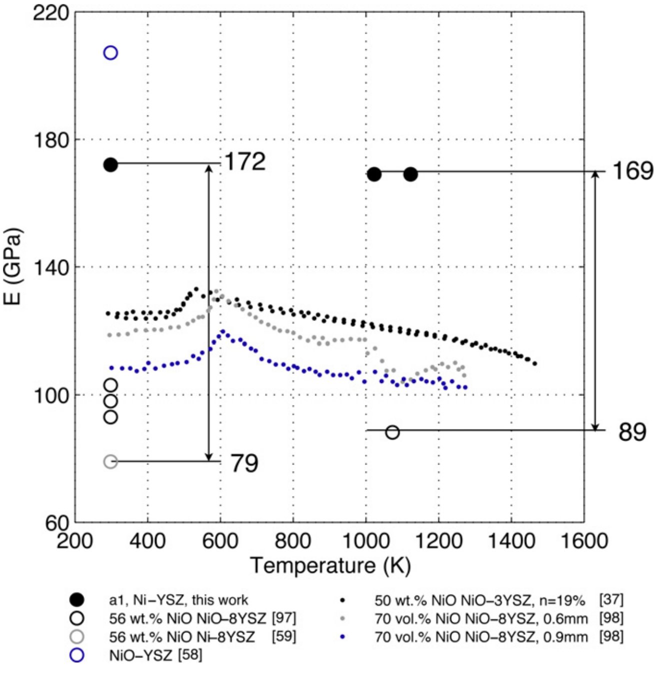

Fig. 8. Temperature dependent Young modulus of the anode in oxidised state [37,59,58,97,98]. (For interpretation of colour in the artwork the reader is referred to the web version of the article.)

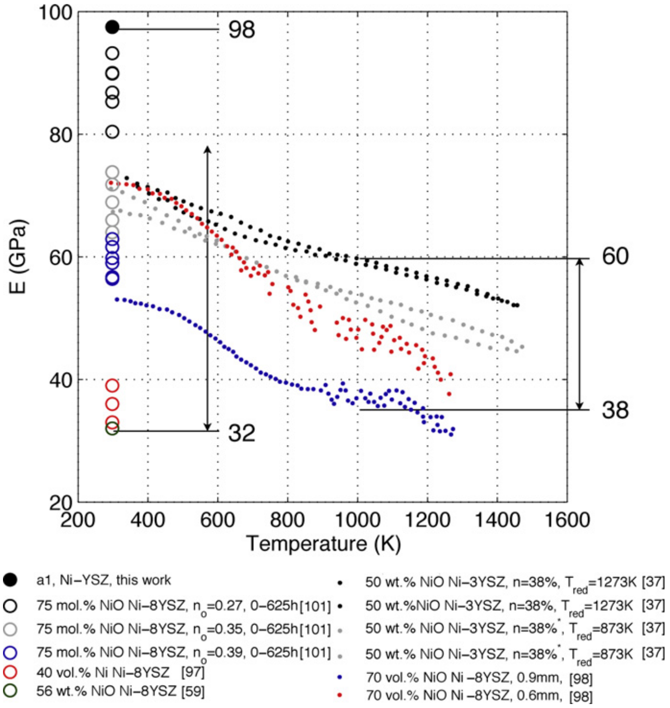

Fig. 9. Temperature dependent Young modulus of the anode in reduced state [37,59,97,101,98]. (For interpretation of colour in the artwork the reader is referred to the web version of the article.)

temperature. The values measured at room temperature in the present study are consistent with previous ones, though slightly lower, as the porosity of the investigated anodes is known to be around 0.25 in reduced state [5], which would yield a very low initial porosity of 0.026, after conversion by Eq. (13). The Young's modulus in oxidised state exhibits a peak related to the antiferromagnetic to paramagnetic transition of NiO, already reflected in the CTE, followed by a decline, though a shift in temperature appears when comparing data between [37] and [98]. The range of reported variations in Young moduli for the common effective anode compositions is large, between 79 and 207 GPa for NiO–YSZ and 18–98 GPa for the reduced anode. This is mainly due to the different porosities, ranging from approximately 25% to 50% in reduced state. The values for a same material at room and operation temperature are comparable. The dependence on the thickness of the sample observed by Biswas et al. [98] is partially accounted for by the bilayer structure. Hence, these measurements are not strictly comparable to the others depicted in Figs. 8 and 9. The drastic drop of the Young's modulus of reduced anodes compared with oxidised ones is attributed to the significant increase in porosity after reduction. Variations in the reduction temperature result in different microstructures. Fig. 9 depicts the temperature-dependence of two samples reduced at 873 K and 1273 K. The behaviour remains qualitatively the same, but a difference of 8 GPa occurs at high temperature. The lower reduction temperature limits the sintering of the Ni particle and results in a finer microstructure [37]. Table 2 lists values of the Poisson's coefficients.

Table 6
Parameters for the assessment of the dependence of the characteristic strength of anode materials at room temperature. Values corresponding to the standard deviation is provided inside the brackets.

Material	σ_{0-0}	b_σ	
NiO–YSZ (75 mol% NiO)	473.4 [369.1; 577.7]	5.12 [4.45; 5.79]	[40]
Ni–YSZ (75 mol% NiO)	158.7 [150.0; 167.4]	2.58 [2.24; 2.92]	[40]

The strength of the anode cermet has received much attention once the effort on the anode-supported arrangement increased in order to reduce the operating temperature. Nonetheless the amount of data on the strength in the most relevant conditions, i.e. at high temperature and in reduced state, is limited because of the required testing apparatus and efforts. The reduction itself, as well as the conditions during this procedure influence the defect population in the reduced anode. For example, an increase in reduction temperature from 873 K to 1273 K was found to enhance the strength at room temperature of Ni–YSZ samples [99]. Radovic et al. [40] proposed an empirical relation between porosity and strength, the parameters of which for both reduced and oxidised materials, are listed in Table 6:

$$\sigma_o = \sigma_{o-o} \exp(-b_\sigma n) \tag{14}$$

The strength at full density is higher for Ni–YSZ, indicating that the decrease is mainly due to the additional porosity. The fractography analysis by Radovic et al. [40] showed a change in the fracture propagation mode upon reduction, from mostly transgranular to intergranular. Even though the porous nature of the material complicates the fractography analysis, typical critical defects could be identified: NiO clusters, which transformed into large foamy nickel structures upon reduction, cavities, surface singularities and YSZ agglomerates. In the case of oxidised specimens, the analysis of the dependence of the estimated Weibull parameters on the thickness of the sample suggests that the strength is controlled by surface defects, the size of which exceeds that of the pore. The dependence of the strength on porosity arises from that of the Young modulus.

Table 7 list the Weibull parameters and strength of Ni(O)–YSZ compiled from the literature. Malzbender et al. [97] reported a decrease in the strength of Ni–YSZ with increasing temperature for both oxidised and reduced state, which is confirmed by our measurements. They also performed the sole study of the strength of SOFC materials by means of the three-parameter Weibull distribution. The two-parameter distribution yielded significantly higher Weibull moduls and resulted in conservative but still misleading predictions of the failure stress for larger components [100]. Grahl-Madsen et al. [92] noted a qualitative relation between reduction strain and strength, as both are dependent on the properties of the YSZ backbone.

There are many evidences of the microstructure alteration of the anode during operation, among which the coarsening of the Ni particles is the most striking from a mechanical point of view. This phenomenon induces a sensible decrease of the effective TPBL, hence the electrochemical performance

Table 7
Weibull parameters and strength of both oxidised and reduced anodes. Inside brackets is the 95% confidence interval.

Material	Composition	Aging/ cycling	Aging condition/ reduction	$T_{measure}$ (K)	n	Method	σ_o/MOR (MPa)	m	Samples	$\mathcal{V}_r$ (mm^3)	
NiO–8YSZ	a1	–	–	RT	–	ROR	290 [277; 304]	6.81 [5.37; 8.63]	30	10.106	This work
NiO–8YSZ	a1	–	–	1073	–	ROR	253 [242; 266]	6.6 [5.16; 8.44]	30	10.694	This work
Ni–8YSZ/8YSZ	75 mol% NiO	0 h	1073 K 4% H_2 96% Ar	RT	39.4	ROR	106.5 [94.6; 118.9]	5.7 [3.5; 8.6]	–	6.239	[101]
Ni–8YSZ/8YSZ	75 mol% NiO	625 h	1073 K 4% H_2 96% Ar	RT	38.8	ROR	87.1 [94.3; 80.1]	7.9 [5; 11.5]	–	4.012	[101]
Ni–8YSZ/8YSZ	75 mol% NiO	0 h	1073 K 4% H_2 96% Ar	RT	35.5	ROR	95.9 [83.6; 110]	5.3 [3.5; 7.9]	–	7.415	[101]
Ni–8YSZ/8YSZ	75 mol% NiO	625 h	1073 K 4% H_2 96% Ar	RT	35.0	ROR	90.72 [82.3; 98.8]	9.5 [6.4; 14]	–	3.391	[101]
Ni–8YSZ/8YSZ	75 mol% NiO	0 h	1073 K 4% H_2 96% Ar	RT	27.4	ROR	127 [117.5; 136.6]	8.6 [5.4; 12.6]	–	4.082	[101]
Ni–8YSZ/8YSZ	75 mol% NiO	625 h	1073 K 4% H_2 96% Ar	RT	26.7	ROR	136.6 [123.4; 151.2]	6.2 [4.1; 9.5]	–	6.312	[101]
Ni–8YSZ/8YSZ	75 mol% NiO	1 cycl.	1073 K 4% H_2 96% Ar	RT	39.5	ROR	90.7 [83.3; 98.2]	7.9 [4.8; 11.9]	–	4.014	[101]
Ni–8YSZ/8YSZ	75 mol% NiO	25 cycl.	1073 K 4% H_2 96% Ar	RT	40.2	ROR	85.8 [74.1; 99.4]	4.1 [2.6; 6.2]	–	9.867	[101]
Ni–8YSZ/8YSZ	75 mol% NiO	250 cycl.	1073 K 4% H_2 96% Ar	RT	40.2	ROR	79.9 [69.4; 92]	4.2 [2.8; 6.6]	–	9.540	[101]
Ni–8YSZ/8YSZ	75 mol% NiO	1250 cycl.	1073 K 4% H_2 96% Ar	RT	39.5	ROR	81.8 [74.1; 89.9]	6.7 [4.1; 9.9]	–	5.005	[101]
Ni–8YSZ/8YSZ	75 mol% NiO	1 cycl.	1073 K 4% H_2 96% Ar	RT	33.9	ROR	126 [115.4; 137]	7.5 [4.7; 11]	–	4.622	[101]
Ni–8YSZ/8YSZ	75 mol% NiO	25 cycl.	1073 K 4% H_2 96% Ar	RT	34.1	ROR	126.6 [112.6; 142.4]	5.1 [3.5; 7.5]	–	7.810	[101]
Ni–8YSZ/8YSZ	75 mol% NiO	250 cycl.	1073 K 4% H_2 96% Ar	RT	34.6	ROR	108.18 [96.1; 120.8]	5.7 [3.5; 8.4]	–	6.703	[101]
Ni–8YSZ/8YSZ	75 mol% NiO	1250 cycl.	1073 K 4% H_2 96% Ar	RT	34.9	ROR	108.3 [98.9; 117.9]	7.3 [4.5; 10.9]	–	4.795	[101]
Ni–8YSZ/8YSZ	75 mol% NiO	1 cycl.	1073 K 4% H_2 96% Ar	RT	26.6	ROR	151.2 [136; 167.1]	6.3 [3.8; 9.3]	–	6.176	[101]
Ni–8YSZ/8YSZ	75 mol% NiO	25 cycl.	1073 K 4% H_2 96% Ar	RT	26.2	ROR	166.1 [151.3; 182.3]	6.4 [4.2; 9.9]	–	6.043	[101]
Ni–8YSZ/8YSZ	75 mol% NiO	250 cycl.	1073 K 4% H_2 96% Ar	RT	26.4	ROR	162.3 [147.2; 177.7]	6.9 [4.3; 10.1]	–	5.462	[101]
Ni–8YSZ/8YSZ	75 mol% NiO	1250 cycl.	1073 K 4% H_2 96% Ar	RT	27.0	ROR	161.5 [144.9; 178.7]	6.9 [3.8; 9.3]	–	5.464	[101]
NiO–8YSZ	75 mol% NiO	–	–	RT	6.6	ROR	134.6 [125.6; 143.6]	8.6 [5.6; 12.1]	15	3.728	[40]
NiO–8YSZ	75 mol% NiO	–	–	RT	17.8	ROR	97.6 [86.4; 110.2]	4.3 [2.9; 6.4]	15	9.549	[40]
NiO–8YSZ	75 mol% NiO	–	–	RT	19.8	ROR	92.1 [84.5; 100.0]	6.8 [4.3; 9.8]	15	5.103	[40]
NiO–8YSZ	75 mol% NiO	–	–	RT	21.9	ROR	95.4 [83.3; 109.1]	4.0 [2.6; 6.0]	15	10.575	[40]
NiO–8YSZ	75 mol% NiO	–	–	RT	22.7	ROR	96.2 [89.9; 111.5]	3.6 [2.4; 5.4]	15	6.124	[40]
NiO–8YSZ	75 mol% NiO	–	–	RT	21.6	ROR	97.2 [77.5; 122.0]	3.2 [1.7; 5.8]	15	22.393	[40]
Ni–8YSZ	75 mol% NiO	–	1073 K 4% H_2 96% Ar	RT	27.4	ROR	115.2 [104.2; 126.2]	6.1 [3.9; 8.7]	15	5.760	[40]
Ni–8YSZ	75 mol% NiO	–	1073 K 4% H_2 96% Ar	RT	36.1	ROR	79.1 [73.2; 85.4]	7.0 [4.8; 10.1]	15	4.812	[40]
Ni–8YSZ	75 mol% NiO	–	1073 K 4% H_2 96% Ar	RT	36.9	ROR	73.5 [66.1; 81.8]	5.0 [3.5; 7.2]	15	7.628	[40]
Ni–8YSZ	75 mol% NiO	–	1073 K 4% H_2 96% Ar	RT	39.8	ROR	55.42 [49.2; 62.5]	4.5 [3.1; 6.5]	15	8.855	[40]
Ni–8YSZ	75 mol% NiO	–	1073 K 4% H_2 96% Ar	RT	39.3	ROR	55.4 [49.2; 62.5]	4.5 [3.1; 6.5]	15	4.377	[40]
Ni–8YSZ	75 mol% NiO	–	1073 K 4% H_2 96% Ar	RT	41.8	ROR	49.5 [45.4; 53.7]	6.4 [4.2; 9.6]	15	8.633	[40]
NiO–8YSZ	56 wt.% NiO	–	–	RT	–	4PB	9.1[a]	25.9	6–10[b]	47.200	[92]
NiO–8YSZ	56 wt.% NiO	–	–	RT	–	4PB	9.6[a]	4.6	6–10[b]	57.000	[92]
NiO–8YSZ	56 wt.% NiO	–	–	RT	–	4PB	9.5[a]	8.2	6–10[b]	56.000	[92]
NiO–8YSZ	56 wt.% NiO	–	–	RT	–	4PB	24.4[a]	14.4	6–10[b]	49.500	[92]
NiO–8YSZ	56 wt.% NiO	–	–	RT	–	4PB	13.4[a]	7.7	6–10[b]	58.400	[92]
NiO–8YSZ	56 wt.% NiO	–	–	RT	–	4PB	20.3[a]	11.5	6–10[b]	55.300	[92]
Ni–8YSZ	56 wt.% NiO	50 h	1123 K 9% H_2 91% Ar	RT	–	4PB	17.5[a]	5.1	6–10[b]	–	[92]
NiO–YSZ/8YSZ	40 vol.% Ni[b]	–	–	RT	–	ROR[d]	115.0[e]	13.2[f]	–	9.734[d]	[97]
NiO–YSZ/8YSZ	40 vol.% Ni[b]	–	–	1073	–	ROR[d]	84.0[e]	13.2[f]	–	9.734[d]	[97]
Ni–YSZ/8YSZ	40 vol.% Ni[b]	–	–	RT	–	ROR[d]	84.0[e]	13.2[f]	–	9.734[d]	[97]
Ni–YSZ/8YSZ	40 vol.% Ni[b]	–	–	1073	–	ROR[d]	67.0[e]	13.2[f]	–	9.734[d]	[97]
Ni–YSZ/8YSZ	40 vol.% Ni[b]	1800 h/40 cycl.	Stack operation	RT	–	ROR[d]	80.6[e]	13.2[f]	–	9.734[d]	[97]
NiO–8YSZ/8YSZ	40 vol.% Ni[b]	–	–	RT	–	ROR[d]	62 [61; 63]	10 [9; 12]	180	8.946[d]	[100]

NiO–8YSZ/8YSZ	40 vol.% Ni[b]	–	–	RT	–	ROR[d]	61 [60; 62][c]	4.8 [4.4; 5.2]	180	–	[100]
NiO–YSZ	75 mol% NiO	–	–	RT	10–14	ROR	187	11.8	10	0.577	[60]
Ni–3YSZ	56 wt.% NiO	–	1273 K, 4 h, 9% H_2 91% N_2	RT	30	ROR	361	11.01	35	0.846	[99]
Ni–3YSZ	56 wt.% NiO	–	873 K, 24 h, 9% H_2 91% N_2	RT	30	ROR	318	9.98	35	0.846	[99]
NiO–3YSZ	56 wt.% NiO	–	–	RT	11	tensile	179	12.7	30	388	[124]
NiO–3YSZ	56 wt.% NiO	–	–	RT	11	BOR	498	8.9	30	0.0064	[124]

[a] 50% value.

[b] Estimated value.

[c] 3-parameter distribution, $\sigma_u = 26[25 ; 27]$ MPa.

[d] Plates tested instead of discs.

[e] MOR.

[f] Averaged value over all tested samples (116).

[8,5,6,76]. Subsequent alteration of the mechanical properties can occur, as strength and creep are strongly dependent on the grain size. Moreover, particular attention is required for composites made of materials displaying different mechanical behaviours subjected to thermal cycling. Different authors observed an increase of the CTE of the Ni–YSZ material upon thermal cycling. Mori et al. [36] report a more severe alteration with increasing heating/cooling rates and denser samples. The effect is larger during the first 5–10 cycles, approximately 4.67×10^{-8} and 5.75×10^{-8} per cycle for 2 K min^{-1} and 10 K min^{-1} heating ramps, respectively, between 323 K and 1273 K. It then reduces to 4.28×10^{-9} and 5.5×10^{-9} per cycle. The difference between cooling and heating measurements indicates a shrinkage of the anode, which is more pronounced during the first cycles. Sun et al. [96] report a similar value of 1.2×10^{-8} (1.4×10^{-8} on average for [36]) for cycling between 298 K and 1173 K. The explanation proposed by Mori et al. [36], i.e. microcracks in the YSZ backbone, does not comply with the observation of Lara-Curzio et al. [101]. The latter have not observed any decrease in Young modulus during overall harsher cycling conditions, nor modification of the porosity, except for one class of specimens.

Lara-Curzio et al. [101] observed a slight but not significant trend in the evolution of the characteristic strength of their Ni–YSZ samples upon thermal cycling. The characteristic strength of the samples with a porosity of approx. 0.34 and 0.4 (0.26) decreased (increased), but all the variations lie within the 95 % confidence interval. Other results from the literature [97] exhibit opposite trends. Extensive research to find the exact underlying phenomena of these discrepancies has not yet been performed.

The creep behaviour of the Ni–YSZ anode is expected to dominate that of anode-supported cells, for geometrical and material reasons. Indeed, the creep strain rate in the anode is the highest among the cell layers, in their respective expected stress range (see Fig. 5). Relatively few studies have been carried out, with inconsistent conclusions among them. The study of Gutierrez-Mora et al. [38] on the compressive creep of standard Ni–8YSZ/8YSZ supports at high temperature (1273–1473 K) highlights a behaviour controlled by the Ni phase at 1373 K. The complex dependences, in particular of the stress exponent on temperature, prevent a reasonable extrapolation of their data to typical SOFC operating temperatures. Morales-Rodriguez et al. [39] investigated in more details a similar material in a similar temperature range, 20–40 vol.% Ni–3YTZP but with a different microstructure than SOFC anodes. Their main finding is that the 3YTZP matrix is the creep-controlling phase, which diametrically differs from that of Gutierrez-Mora et al. [38]. Changes in stress exponents and activation energies occur depending on investigated stresses, temperatures and amount of irreversible strains. Analyses of bending creep test of Ni–8YSZ anode at intermediate SOFC temperature (973–1123 K) by Laurencin et al. [68] further support the predominant role of the YSZ backbone on the overall behaviour. The activation energy for Ni–YSZ (115 kJ mol^{-1}) is much lower than for dense 8YSZ samples (320–370 kJ mol^{-1}). It is closer to values reported for plasma-deposited YSZ thermal barrier coating, the porosity of which is in the range of 15% [102]. This suggests a change in the creep controlling mechanisms, from cation bulk diffusion to cation surface diffusion [68]. Table 4 proposes a set of parameters for Eq. (10). Fig. 5 shows that the parameters for 40 vol.% Ni–3YTZP provides a reasonable match with the high temperature data from Gutierrez-Mora et al. [38] and can be used, despite the likely difference in materials, for preliminary analyses of stress relaxation in the cell, during the cooldown after the sintering step. In operation, the parameters determined by Laurencin et al. [68] should be used.

4.3. Cathode

Anode-supported cells mostly differ in the choice of the cathode. LSM has been used for a long time and has proved its stability during operation at high-temperature. The use of a LSM–YSZ composite has enabled a considerable improvement of the performance [103], hence reduction of the operating temperature. LSCF cathodes combined to YDC or GDC compatibility layers are the result of concurrent research on more reactive materials. The oxygen reduction reaction proceeds differently in LSM or LSCF-based electrodes [104]. The same applies to the possible mechanisms of failure since the CTEs of both types of material differ significantly, as depicted in Figs. 10 and 11.

Higher Sr content on the A-site increases the CTE of $La_{1-x}Sr_xMnO_3$, though the dependence on the Sr content inverts around $x = 0.1$, as reported by Mori et al. [81]. They observed different structures and phase transformations, depending on the Sr content, which, however, did not result in anomalies in the CTEs.

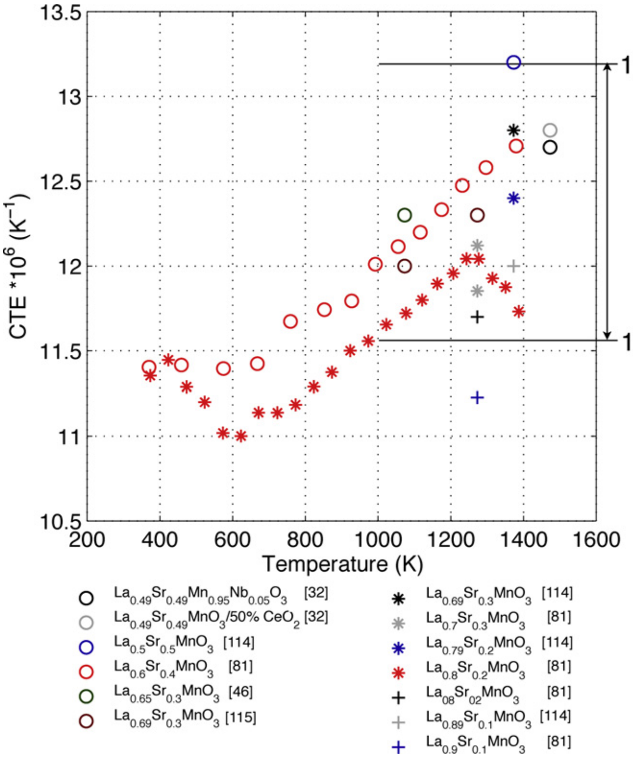

Fig. 10. Temperature dependent CTEs of LSM [32,46,114,115,81]. (For interpretation of colour in the artwork the reader is referred to the web version of the article.)

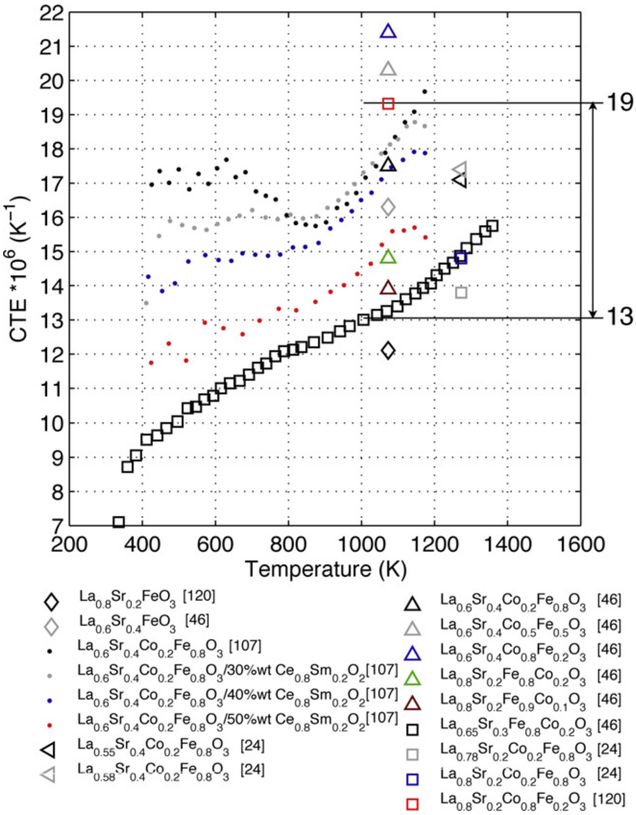

Fig. 11. Temperature dependent CTEs of LSCF and LSF [24,46,107,120]. (For interpretation of colour in the artwork the reader is referred to the web version of the article.)

Tai et al. [105,106] studied the CTE of $La_{1-x}Sr_xCo_{1-y}Fe_yO_3$, depending on the Sr and Fe content. For $x = 0.2$ (LSCF82$(1-y)y$), the CTE increases upon higher Co content, up to $y = 0.4$, then stays constant. Higher Sr content x in LSCF$(1-x)x28$ ($y = 0.8$) increases the CTE. These materials do not exhibit any CTE hysteresis in air. There is a reversible transition close to 923 K, due to the formation of oxygen vacancies and concurrent reduction of the Fe and Co ions. The magnitude of the oxygen loss, consequently contribution of chemical expansion, increases with higher Sr or Co content, while the threshold temperature decreases. Similar to the LSM case, different phases and transitions occur, depending on the Sr or Fe content, though the magnitude of their influence on the CTE is again limited. The threshold temperature of the orthorhombic to rhombohedral transition decreases with increased Sr content on the A-site, while only the rhombohedral phase is observed for Fe contents lower than 0.7. Xu et al. [107] reported similar trends. Their measurements on composite LSCF-SDC cathodes indicate a decrease of the threshold temperature for the change in differential CTE and mismatch in CTE with other SOFC layers.

The data on the elastic properties of cathode SOFC materials is scarce, not to mention the temperature dependence. Most of the measurements are performed on dense samples, not reflecting the microstructure of a porous functional cathode.

Ferroelastic behaviour, or observations in line with such behaviour, has been reported for both LSM [30] and LSCF [43]. It has been studied extensively for other perovskite materials, such as $LaCoO_3$ and is characterized by hysteresis in the stress–strain relationship during loading and unloading cycles because of domain switching resulting in strain [108,109]. Permanent deformation is therefore generated when the sample is loaded, even at room temperature as observed during four-point bend tests [30,43]. Care is needed when considering data on the Young's modulus deduced from the stress–strain curves [43]. For LSM, Meixner et al. [30] suggest the uptake of oxygen at high temperature during cooling influences the ferroelastic behaviour, owing to the strong dependence on the processing history, mainly cooling rate and sample thickness. Higher amount of permanent deformation was obtained by increasing the Sr content from 0.3 to 0.5. Lein et al. [43] identified a ferroelastic to paraelastic transition for $La_{0.5}Sr_{0.5}Co_{0.5}Fe_{0.5}O_3$ and $La_{0.5}Sr_{0.5}Co_{0.25}Fe_{0.75}O_3$ around 573 K, above which the behaviour is elastic, to the limit of possible creep deformation. The amount of data found in the literature on the mechanical behaviour of the common cathode perovskite materials used in anode-supported SOFCs is not sufficient to deduce detailed temperature and conditions dependent constitutive laws that include the ferroelastic behaviour. This warrants further investigations to precisely understand and identify the failure modes on the cathode side. The available data is reported hereafter.

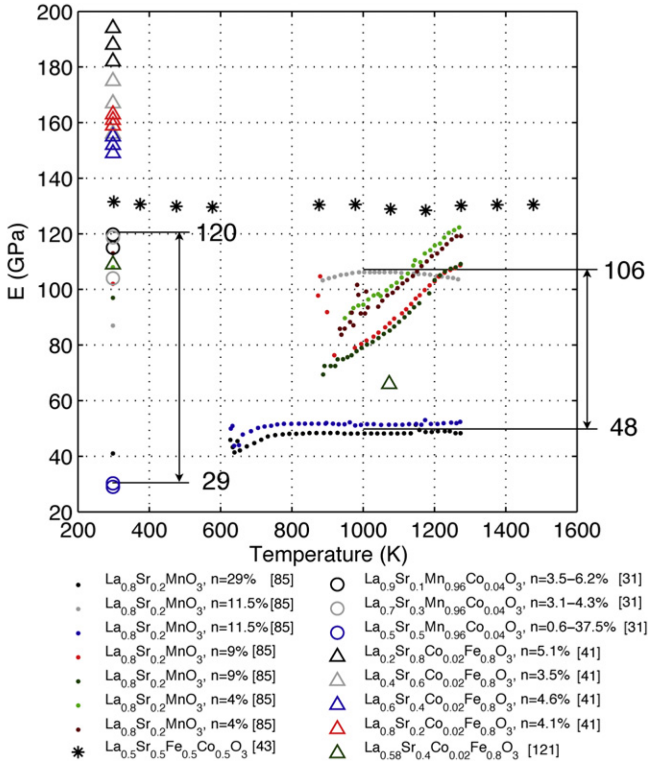

Fig. 12. Young modulus of LSM and LSCF [41,85,121,31,43]. (For interpretation of colour in the artwork the reader is referred to the web version of the article.)

The Young's modulus of LSM samples measured by Giraud et al. [85] exhibits singularities. Impulse excitation measurements could not be performed for temperatures lower than 623 K and 873 K for porous and dense samples, respectively, presumably because of their ability to absorb vibrations. At higher temperatures, the Young's modulus of the porous samples remains fairly constant, while that of dense samples increases monotonically (see Fig. 12). No explanation is provided for this behaviour. Fig. 12 depicts the Young's moduli of dense LSCF materials, which slightly increases with Sr content [41] and stays fairly constant between room temperature and 1073 K [43]. Reported Poisson's ratios are listed in Table 2.

Table 8
Weibull parameters and strength of cathode materials. Inside bracket is the standard deviation.

Material	Composition	Aging	T_{msrmt} (K)	n (%)	Method	σ_o or MOR (MPa)	m	Samples	$\mathcal{V}_r$ (mm^3)	
LSM	$La_{0.8}Sr_{0.2}SrO_3$	–	298	10–15	ROR	52	6.7	10	1.217	[60]
LSM	$La_{0.8}Sr_{0.2}SrO_3$	–	1073	10–15	ROR	75	3.7	10	2.836	[60]
LSM	$La_{0.49}Sr_{0.49}Mn_{0.95}Nb_{0.05}O_3$	–	298	0.5–1.5	BOR	138	15	20^a	0.341	[32]
GDC	$Ce_{0.845}Gd_{0.15}Co_{0.005}O_3$	–	298	0.5–1.5	BOR	497	3.6	9^a	2.199	[32]
LSM–GDC	30vol.% GDC	–	298	2–8.5	BOR	383	8.5	19^a	0.683	[32]
LSM	$La_{0.5}Sr_{0.5}Mn_{0.95}Nb_{0.05}O_3$	–	298	0.5–1.5	BOR	130	11	14	0.510	[30]
LSM	$La_{0.9}Sr_{0.1}Mn_{0.95}Nb_{0.05}O_3$	–	298	–	BOR	242	14	14	0.378	[30]
LSCF	$La_{0.5}Sr_{0.5}Fe_{0.5}Co_{0.5}O_3$	–	298	3	4PB	107 [92; 122]	–	11	–	[43]
LSCF	$La_{0.5}Sr_{0.5}Fe_{0.5}Co_{0.5}O_3$	773 K, 500 h	298	3	4PB	121 [114; 128]	–	5	–	[43]
LSCF	$La_{0.5}Sr_{0.5}Fe_{0.5}Co_{0.5}O_3$	–	1073	3	4PB	181 [168; 194]	–	5	–	[43]
LSCF	$La_{0.5}Sr_{0.5}Fe_{0.5}Co_{0.5}O_3$	773 K, 500 h	298	5	4PB	128 [116; 140]	–	8	–	[43]
LSCF	$La_{0.5}Sr_{0.5}Fe_{0.5}Co_{0.5}O_3$	–	1073	5	4PB	166 [151; 181]	–	6	–	[43]
LSCF	$La_{0.5}Sr_{0.5}Fe_{0.5}Co_{0.5}O_3$	–	1273	5	4PB	181 [158; 204]	–	5	–	[43]
LSCF	$La_{0.5}Sr_{0.5}Fe_{0.25}Co_{0.75}O_3$	–	298	5	4PB	71 [64; 78]	–	6	–	[43]
LSCF	$La_{0.5}Sr_{0.5}Fe_{0.25}Co_{0.75}O_3$	773 K, 500 h	673	3	4PB	61 [41; 81]	–	3	–	[43]
LSCF	$La_{0.5}Sr_{0.5}Fe_{0.25}Co_{0.75}O_3$	773 K, 500 h	873	3	4PB	121 [110; 132]	–	3	–	[43]
LSCF	$La_{0.5}Sr_{0.5}Fe_{0.25}Co_{0.75}O_3$	–	1073	3	4PB	120 [109; 131]	–	5	–	[43]
LSF	$La_{0.5}Sr_{0.5}FeO_3$	–	298	1	4PB	138 [126; 150]	–	8	–	[43]
LSF	$La_{0.5}Sr_{0.5}FeO_3$	–	1073	1	4PB	181 [163; 199]	–	6	–	[43]

[a] Estimated value.

Data on the strength of cathode materials mostly consists in flexural bending strength for dense materials. Studies including the effect of correcting the measurements for the non-linear stress–strain response of these ferroelastic materials could not be found. Compiled values of the Weibull parameters are listed in Table 8. Atkinson et al. [60] report a low strength for $La_{0.8}Sr_{0.2}MnO_3$, without explanation and similar to GDC (Section 4.1), the characteristic strength increases with temperature. De Souza et al. [29] have observed an overall increase of the flexural strength of $La_{0.875}Sr_{0.125}MnO_3$ from RT to 1273 K, a minimum being located around 673 K. They suggest that this behaviour is driven by variations in symmetry due to first the phase transition from orthorhombic to rhombohedral around 523–623 K and then temperature dependence of the symmetry of the crystal lattice, and oxygen stoichiometry accommodated by the oxidation of Mn^{3+} to Mn^{4+}. Similar trends in the temperature dependence of the flexural strength of $La_{0.5}Sr_{0.5}MnO_3$ is observed [30]. Weibull data for LSCF materials is difficult to find. The samples studied by Chou et al. [41] are weaker for higher strontium contents, but the manufacturing of crack-free specimens could not be achieved for the highest Sr contents. The flexural bending strength of $La_{0.5}Sr_{0.5}Co_{0.5}Fe_{0.5}O_3$ is lower at room temperature than at 1073 K, since a gradient in oxygen content is expected to develop in the sample upon cooling from the sintering temperature, which induces tensile stress on the surfaces because of chemical expansion [43].

Porous $La_{0.6}Sr_{0.4}MnO_3$ samples undergo severe shrinkage during thermal cycling ($5\ K\ min^{-1}$) but not aging in air or oxygen between 873 K and 1373 K [81]. The strain per cycle is as high as 5×10^{-4}. The shrinkage is linked to a severe coarsening of the microstructure.

The data found on the creep behaviour of LSM materials is not relevant in the present framework as its validity is limited to temperatures much higher (1523 K) than those in intermediate-temperature SOFC [110]. In contrast, the study of Lein et al. [111] includes compressive creep of $La_{0.5}Sr_{0.5}Fe_{0.5}Co_{0.5}O_3$ at 1173–1323 K in air. The low stress exponent and comparison of creep and cation diffusion activation energies suggest that creep is controlled by boundary or bulk diffusion of Sr and/or La. Table 4 lists the parameters and Fig. 5 depicts the corresponding computed curves along with a selection of experimental measurements.

5. Conclusion

The present compilation of available data from the literature highlights the pronounced dependence of the mechanical properties of SOFC materials on temperature. The use of temperature-independent values may induce misleading predictions of the stress state in the different cell layers, and hence of the occurrence and of the types of mechanical failures.

It is known that the CTE of YSZ is the lowest among the different materials used in anode-supported SOFC, which lets foresee a residual compressive stress in this layer and tensile residual stress in the anode. The data recorded on the CTE of the latter does not assert that the CTE is higher in reduced than in oxidised state. The situation is less well defined in the other layers, except in LSCF cathodes, which are likely subjected to a tensile stress. Indeed, the CTEs of LSM, YDC or GDC overlap that of the anode. Therefore the stress state can be either tensile or compressive in the layers made of these materials. This underscores the possible occurrence of transitions, depending on temperature and state of the anode. The mechanical behaviour of the anode during its reduction is imprecisely understood. Measurements carried out on unconstrained samples are unlikely to hold for the structural analysis of SOFC stacks, where the reduction step is performed on the whole stack, with uneven temperature and gas distributions. This warrants further investigations.

On the one hand, the data on the elastic properties of YSZ and anode material is fairly exhaustive, even though large variations in microstructures, hence mechanical properties, are possible. Significant and non-linear temperature dependence is observed. Data on the Young's modulus of GDC, YDC, LSM and LSCF in their form in SOFCs is on the other hand very scarce in the literature, if not inexistent. The cathode has a minor effect on the stresses in the other layers of anode-supported cells, but the prediction of its mechanical failure is equally important to improve the reliability of SOFC stacks, without mentioning other cell designs, especially cathode-supported ones. The same applies to the measurement of the strength of SOFCs materials.

The foregoing properties are required for the calculation of stresses in SOFCs, which enable at best a preliminary assessment of possible failures due to aging. Their evolution upon operating time is needed for insights into mechanical degradation. Shrinkage of the anode and cathode materials has been reported during thermal cycling exclusively, while first results indicate that the strength of all materials certainly evolves during SOFC operation. The mechanisms, hence the dependence on SOFC operating conditions, are not precisely understood. Another source of evolution of the stresses in SOFCs during operation is creep. A simple approach can reproduce the correct order of magnitude of the few available data, and can be used in preliminary structural analyses.

Despite all these limitations, the mechanical properties compiled in the present work already allow a reasonably accurate structural analysis of SOFC stacks, which can in turn highlight the most stringent needs in mechanical characterisations.

Acknowledgements

This work was funded by the Swiss SOFC Consortium, co-financed by the Swiss Federal Office of Energy (SFOE), contract number 152210 and Swisselectric Research. Roland Bächtold from EMPA and Enrico G. Tagliaferri from Htceramix are kindly acknowledged for their participation in this work. The author would like to thank warmely Stefan Diethelm (LENI-EPFL) and Shigehisa Kasahara (UNCTAD) for careful reading of the manuscript. gPROMS, a modelling tool from Process System Enterprise (PSE) has been used under academic licensing.

References

[1] Gazzarri, J. Kesler, O. Short-stack modeling of degradation in solid oxide fuel cells. Part I. Contact degradation, Journal of Power Sources 176 (2008) 138–154.

[2] Nakajo, A. Mueller, F. McLarty, D. Brouwer, J. Van herle, J. Favrat, D. The effects of dynamic dispatch on the degradation of solid oxide fuel cell systems, The Journal of The Electrochemical Society 158 (2011) B1329–B1340.

[3] Wuillemin, Z. Autissier, N. Nakajo, A. Luong, M.-T. Van herle, J. Favrat,D. Modeling and study of the influence of sealing on a solid oxide fuel cell, Journal of Fuel Cell Science and Technology 5 (2008) 011016–011019.

[4] Hagen, A. Barfod, R. Hendriksen, P. Liu, Y. Ramousse, S. Degradation of anode supported SOFCs as a function of temperature and current load, Journal of the Electrochemical Society 153 (2006) A1165–A1171.

[5] Faes, A. Hessler-Wyser, A. Presvytes, D. Vayenas, C. Van herle, J. Nickel–zirconia anode degradation and triple phase boundary quantification from microstructural analysis, Fuel Cells 9 (6) (2009) 841–851.

[6] Tanasini, P. Cannarozzo, M. Costamagna, P. Faes, A. Van herle, J. Hessler-Wyser, A. Comninellis, C. Experimental and theoretical investigation of degradation mechanisms by particle coarsening in SOFC electrodes, Fuel Cells 9 (2009) 740–752.

[7] Simwonis, D. Tietz, F. Stöver, D. Nickel coarsening in annealed Ni/8YSZ anode substrates for solid oxide fuel cells, Solid State Ionics 132 (2000) 241–251.

[8] Holzer, L. Iwanschitz, B. Hocker, T. Münch, B. Prestat, M. Wiedenmann, D. Vogt, U. Holtappels, P. Sfeir, J. Mai, A. Graule,T. Microstructure degradation of cermet anodes for solid oxide fuel cells: quantification of nickel grain growth in dry and in humid atmospheres, Journal of Power Sources 196 (2011) 1279–1294.

[9] John, J. Izzo, R. Joshi, A.S. Grew, K.N. Chiu, W.K.S. Tkachuk, A. Wang, S.H. Yun,W. Nondestructive reconstruction and analysis of SOFC anodes using X-ray computed tomography at sub-50 nm resolution, Journal of the Electrochemical Society 155 (2008) B504–B508.

[10] Vels Jensen, K. Primdahl, S. Chorkendorff, I. Mogensen,M. Microstructural and chemical changes at the Ni/YSZ interface, Solid State Ionics 144 (2001) 197–209.

[11] Liu, Y. Jiao,C. Microstructure degradation of an anode/electrolyte interface in SOFC studied by transmission electron microscopy, Solid State Ionics 176 (2005) 435–442.

[12] Backhaus-Ricoult,M. SOFC – a playground for solid state chemistry, Solid State Sciences 10 (2008) 670–688.

[13] Mitterdorfer, A. Gauckler,L.J. $La_2Zr_2O_7$ formation and oxygen reduction kinetics of the $La_{0.85}Sr_{0.15}Mn_yO_3$, O_2(g)YSZ system, Solid State Ionics 111 (1998) 185–218.

[14] Liu, Y. Hagen, A. Barfod, R. Chen, M. Wang, H. Poulsen, F. Hendriksen,P. Microstructural studies on degradation of interface between LSM–YSZ cathode and YSZ electrolyte in SOFCs, Solid State Ionics 180 (2009) 1298–1304.

[15] Chen, M. Liu, Y. Hagen, A. Hendriksen, P. Poulsen,F. LSM–YSZ Reactions in Different Atmospheres, Fuel Cells, 2009.

[16] Hattori, M. Takeda, Y. Sakaki, Y. Nakanishi, A. Ohara, S. Mukai, K. Lee, J. Fukui,T. Effect of aging on conductivity of yttria stabilized zirconia, Journal of Power Sources 126 (2004) 23–27.

[17] Appel, C. Bonanos, N. Horsewell, A. Linderoth, S. Ageing behaviour of zirconia stabilised by yttria and manganese oxide, Journal of Materials Science 36 (2001) 4493–4501.

[18] Atkinson, A. Selçuk, A. Residual stress and fracture of laminated ceramic membranes, Acta Materialia 47 (1999) 867–874.

[19] Deseure, J. Dessemond, L. Bultel, Y. Siebert,E. Modelling of a SOFC graded cathode, Journal of the European Ceramic Society 25 (2005) 2673–2676.

[20] Muller, A. Krugel, A. Weber, A. Ivers-Tiffée, E. Characterization of multilayer anodes for SOFC, in: in: Material Research Society Symposium Proceedings, vol. 756, Materials Research Society, Warrendale, Pa, 1999, pp. 533–538.

[21] Nakajo, A. Wuillemin, Z. Van herle, J. Favrat, D. Simulation of thermal stresses in anode-supported solid oxide fuel cell stacks. Part I. Probability of failure of the cells, Journal of Power Sources 193 (2009) 203–215.

[22] Nakajo, A. Van herle, J. Favrat, D. Sensitivity of stresses and failure mechanisms in SOFCs to the mechanical properties and geometry of the constitutive layers, Fuel Cells 11 (2011) 537–552.

[23] Mai, A. Haanappel, V.A. Uhlenbruck, S. Tietz, F. Stöver, D. Ferrite-based perovskites as cathode materials for anode-supported solid oxide fuel cells. Part I. Variation of composition, Solid State Ionics 176 (2005) 1341–1350.

[24] Mai, A. Haanappel, V.A. Tietz, F. Stöver, D. Ferrite-based perovskites as cathode materials for anode-supported solid oxide fuel cells. Part II. Influence of the CGO interlayer, Solid State Ionics 177 (2006) 2103–2107.

[25] A. Nakajo, F. Mueller, J. Brouwer, J. Van herle, D. Favrat, Mechanical reliability and durability of SOFC stacks. Part II. Modelling of mechanical failures during aging and cycling, International Journal of Hydrogen Energy, under review.

[26] Evans, A. Hutchinson,J. The thermomechanical integrity of thin films and multilayers, Acta Metallurgica et Materialia 43 (1995) 2507–2530.

[27] Nguyen, B. Koeppel, B. Ahzi, S. Khaleel, M. Prabhakar, S. Crack growth in solid oxide fuel cell materials: from disrcete to continuum damage modeling, Journal of American Ceramic Society 89 (2006) 1358–1368.

[28] Kondoh,J. Yttria-fully-stabilized zirconia, Journal of Alloys and Compounds 370 (2004) 285–290.

[29] D'Souza, C. Sammes,N. Mechanical properties of strontium-doped lanthanum manganite, Journal of American Ceramic Society 83 (2000) 47–52.

[30] Meixner, D. Cutler,R. Low-temperature plastic deformation of a perovskite ceramic material, Solid State Ionics 146 (2002) 285–300.

[31] Meixner, D. Cutler,R. Sintering and mechanical characteristics of lanthanum strontium manganite, Solid State Ionics 146 (2002) 273–284.

[32] Cutler, R. Meixner,D. Ceria–lanthanum strontium manganite composites for use in oxygen generation systems, Solid State Ionics 159 (2003) 9–19.

[33] Weibull,W. A statistical theory of the strength of materials, Proceedings of the Royal Swedish Institute of Engineering Research 151 (1939) 1–45.

[34] Kumar, H. Briant, C. Curtin,W. Using microstructure reconstruction to model mechanical behavior in complex microstructures, Mechanics of Materials 38 (2006) 818–832.

[35] Baniassadi, M. Mortazavi, B. Hamedani, H.A. Garmestani, H. Ahzi, S. Fathi-Torbaghan, M. Ruch, D. Khaleel,M. Three-dimensional reconstruction and homogenization of heterogeneous materials using statistical correlation functions and FEM, Computational Materials Science 51 (2012) 372–379.

[36] Mori, M. Yamamoto, T. Itoh, H. Inaba, H. Tagawa,H. Thermal expansion of nickel–zirconia anodes in solid oxide fuel cells during fabrication and operation, Journal of the Electrochemical Society 145 (1998) 1374.

[37] Pihlatie, M. Kaiser, A. Mogensen, M. Mechanical properties of NiO/Ni–YSZ composites depending on temperature, porosity and redox cycling, Journal of the European Ceramic Society 29 (2009) 1657–1664.

[38] Gutierrez-Mora, F. Ralph, J.M. Routbort,J.L. High-temperature mechanical properties of anode-supported bilayers, Solid State Ionics 149 (2002) 177–184.

[39] Morales-Rodriguez, A. Bravo-Leon, A. Dominguez-Rodriguez, A. Lopez-Esteban, S. Moya, J. Jimenez-Melendo,M. High-temperature mechanical properties of zirconia/nickel composites, Journal of the European Ceramic Society 23 (2003) 2849–2856.

[40] Radovic, M. Lara-Curzio,E. Mechanical properties of tape cast nickel-based anode materials for solid oxide fuel cells before and after reduction in hydrogen, Acta Materialia 52 (2004) 5747–5756.

[41] Chou, Y. Stevenson, J. Armstrong, T. Pederson, L. Mechanical properties of $La_{1-x}Sr_xCo_{0.2}Fe_{0.8}O_3$ mixed-conducting perovskites made by the combustion synthesis technique, Journal of American Ceramic Society 83 (2000) 1457–1464.

[42] Selçuk, A. Atkinson,A. Strength and toughness of tape-cast yttria-stabilized zirconia, Journal of American Ceramic Society 83 (2000) 2029–2035.

[43] Lein, H. Andersen, O. Vullum, P. Lara-Curzio, E. Holmestad, R. Einarsrud, M.-A. Grande,T. Mechanical properties of mixed conducting $La_{0.5}Sr_{0.5}Fe_{1-x}Co_xO_{3-\delta}$ ($0 \leq x \leq 1$) materials, Journal of Solid State Electrochemistry 10 (2006) 635–642.

[44] A. S. for Testing, Materials, Standard Test Method for Linear Thermal Expansion of Solid Materials with a Push-Rod Dilatometer, ASTM Standard No. E228-06.

[45] Method A2: Static Flexure Method, EN 843-2.

[46] Ullmann, H. Trofimenko, N. Tietz, F. Stöver, D. Ahmad-Khanlou, A. Correlation between thermal expansion and oxide ion transport in mixed conducting perovskite-type oxides for SOFC cathodes, Solid State Ionics 138 (2000) 79–90.

[47] Hayashi, H. Kanoh, M. Quan, C.J. Inaba, H. Wang, S. Dokiya, M. Tagawa,H. Thermal expansion of Gd-doped ceria and reduced ceria, Solid State Ionics 132 (2000) 227–233.

[48] Yakabe, H. Yasuda,I. Model analysis of the expansion behavior of $LaCrO_3$ interconnector under solid oxide fuel cell operation, Journal of the Electrochemical Society 150 (2003) A35–A45.

[49] Sato, K. Yashiro, K. Kawada, T. Yugami, H. Hashida, T. Mizusaki, J. Fracture process of nonstoichiometric oxide based solid oxide fuel cell under oxidizing/reducing gradient conditions, Journal of Power Sources 195 (2010) 5481–5486.

[50] Atkinson,A. Chemically-induced stresses in gadolinium-doped ceria solid oxide fuel cell electrolytes, Solid State Ionics 95 (1997) 249–258.

[51] Atkinson, A. Ramos,T.M.G.M. Chemically-induced stresses in ceramic oxygen ion-conducting membranes, Solid State Ionics 129 (2000) 259–269.

[52] Pihlatie, M. Frandsen, H. Kaiser, A. Mogensen,M. Continuum mechanics simulations of NiO/Ni–YSZ composites during reduction and re-oxidation, Journal of Power Sources 195 (2010) 2677–2690.

[53] Watanabe, S. Iguchi, F. Mizusaki, J. Sato, K. Yashiro, K. Kawada, T. Takeyama, Y. Hashida,T. Development of in-situ mechanical testing method for SOFC components, in: Proceedings of the ASME 2010 Eighth International Fuel Cell Science, 2010.

[54] Hashida, T. Sato, K. Takeyama, Y. Kawada, T. Mizusaki, J. Deformation and fracture characteristics of zirconia and ceria-based electrolytes for sofcs under reducing atmospheres, ECS Transactions 25 (2009) 1565–1572.

[55] Kharton, V. Marques, F. Atkinson,A. Transport properties of solid oxide electrolyte ceramics: a brief review, Solid State Ionics 174 (2004) 135–149.

[56] ABAQUS Inc., v6.8, Hibbitt, Karlsson and Sorensen, Rhode Island.

[57] Radovic, M. Lara-Curzio, E. Riester,L. Comparison of different experimental techniques for determination of elastic properties of solids, Materials Science and Engineering A 368 (2004) 56–70.

[58] Selcuk, A. Atkinson, A. Elastic properties of ceramic oxides used in solid oxide fuel cells (SOFC), Journal of the European Ceramic Society 17 (1997) 1523–1532.

[59] Sarantaridis, D. Chater, R. Atkinson,A. Changes in physical and mechanical properties of SOFC Ni–YSZ composites caused by redox cycling, Journal of the Electrochemical Society 155 (2008) B467.

[60] Atkinson, A. Selçuk,A. Mechanical behaviour of ceramic oxygen ion-conducting membranes, Solid State Ionics 134 (2000) 59–66.

[61] Kuebler, J. Primas, R. Gut,B. Mechanical strength of thermally aged and cycled thin zirconia sheets, Advances in Science & Technology 3 B (1994).

[62] A. S. for Testing, Materials, Standard Test Method for Monotonic Equibiaxial Flexural Strength of Advanced Ceramics at Ambient Temperature, ASTM Standard C1499-04.

[63] Kao, R. Perrone, N. Capps,W. Large-deflection solution of the coaxial-ring-circular-glass-plate flexure problem, Journal of the American Ceramic Society 54 (1971) 566–571.

[64] Selçuk, A. Atkinson, A. Strength and toughness of tape-cast yttria-stabilized zirconia, Journal of American Ceramic Society 83 (2000) 2029–2035.

[65] MATLAB, v7.5, The Mathworks Inc., Natik.

[66] Wereszczak, A.A. Ferber, M.K. Kirkland, T.P. Barnes, A.S. Frome, E.L. Menon, M.N. Asymmetric tensile and compressive creep deformation of hot-isostatically-pressed Y_2O_3-doped -Si_3N_4, Journal of the European Ceramic Society 19 (1999) 227–237.

[67] Ding,J.L. Numerical study of the time dependent behavior of GN-10 structural ceramics in bend creep test, Journal of Materials Science 37 (2002) 4165–4180.

[68] Laurencin, J. Delette, G. Usseglio-Viretta, F. Iorio, S.D. Creep behaviour of porous SOFC electrodes: measurement and application to Ni–8YSZ cermets, Journal of the European Ceramic Society 31 (2011) 1741–1752.

[69] Oppenheimer, S.M. Dunand,D.C. Finite element modeling of creep deformation in cellular metals, Acta Materialia 55 (2007) 3825–3834.

[70] Barsoum, M. Fundamentals of Ceramics, Taylor & Francis, 2003.

[71] Gibson, L. Ashby, M. Cellular Solids: Structure and Properties, Cambridge University Press, 1999.

[72] Choe, H. Dunand, D.C. Mechanical properties of oxidation-resistant Ni–Cr foams, Materials Science and Engineering A 384 (2004) 184–193.

[73] Kondoh, J. Kawashima, T. Kikuchi, S. Tomii, Y. Ito, Y. Effect of aging on yttria-stabilized zirconia. 1. A study of its electrochemical properties, Journal of the Electrochemical Society 145 (1998) 1527–1536.

[74] Kondoh, J. Kikuchi, S. Tomii, Y. Ito, Y. Effect of aging on yttria-stabilized zirconia. 2. A study of the effect of the microstructures on conductivity, Journal of the Electrochemical Society 145 (1998) 1536–1550.

[75] Kondoh, J. Kikuchi, S. Tomii, Y. Ito, Y. Effect of aging on yttria-stabilized zirconia, Journal of the Electrochemical Society 145 (1998) 1550–1560.

[76] Nakajo, A. Tanasini, P. Diethelm, S. Van herle, J. Favrat, D. Electrochemical model of solid oxide fuel cell for simulation at the stack scale ii: implementation of degradation processes, Journal of the Electrochemical Society 158 (2011) B1102–B1118.

[77] Lin, C.-K. Chen, T.-T. Chyou, Y.-P. Chiang, L.-K. Thermal stress analysis of a planar SOFC stack, Journal of Power Sources 164 (2007) 238–251.

[78] Fardadi, M. Mueller, F. Jabbari,F. Feedback control of solid oxide fuel cell spatial temperature variation, Journal of Power Sources 195 (2010) 4222–4233.

[79] A. Nakajo, F. Mueller, J. Brouwer, J. Van herle, D. Favrat, Progressive activation of degradation processes in SOFC stacks. Part I. Lifetime extension by optimisation of the operating conditions, Journal of the Electrochemical Society, in preparation.

[80] Hayashi, H. Saitou, T. Maruyama, N. Inaba, H. Kawamura, K. Mori,M. Thermal expansion coefficient of yttria stabilized zirconia for various yttria contents, Solid State Ionics 176 (2005) 613–619.

[81] Mori, M. Hiei, Y. Sammes, N. Tompsett, G. Thermal-expansion behaviors and mechanisms for Ca- or Sr-doped lanthanum manganite perovskites under oxidizing atmospheres, Journal of the Electrochemical Society 147 (2000) 1295.

[82] Adams, J. Young's modulus, flexural strength, and fracture of yttria-stabilized zirconia versus temperature, Journal of the American Ceramic Society 80 (2000) 903–908.

[83] Roebben, G. Basu, B. Vleugels, J. Van der Biest,O. Transformation-induced damping behaviour of Y–TZP zirconia ceramics, Journal of the European Ceramic Society 23 (2003) 481–489.

[84] Weller, M. Herzog, R. Kilo, M. Borchardt, G. Weber, S. Scherrer,S. Oxygen mobility in yttria-doped zirconia studied by internal friction, electrical conductivity and tracer diffusion experiments, Solid State Ionics 175 (2004) 409–413.

[85] Giraud, S. Canel,J. Young's modulus of some SOFCs materials as a function of temperature, Journal of the European Ceramic Society 28 (2008) 77–83.

[86] Kushi, T. Sato, K. Unemoto, A. Hashimoto, S. Amezawa, K. Kawada,T. Elastic modulus and internal friction of SOFC electrolytes at high temperatures under controlled atmospheres, Journal of Power Sources 196 (2011) 7989–7993.

[87] Lowrie, F. Rawlings,R. Room and high temperature failure mechanisms in solid oxide fuel cell electrolytes, Journal of the European Ceramic Society 20 (2000) 751–760.

[88] Ishida, T. Iguchi, F. Sato, K. Hashida, T. Yugami,H. Fracture properties of $(CeO_2)_{1-x}(RO_{1.5})_x$ (R = Y, Gd, and Sm; $x = 0.02$–0.20) ceramics, Solid State Ionics 176 (2005) 2417–2421.

[89] Haering, C. Roosen, A. Schichl, H. Degradation of the electrical conductivity in stabilised zirconia systems. Part I. Yttria-stabilised zirconia, Solid State Ionics 176 (2005) 253–259.

[90] Lakki, A. Herzog, R. Weller, M. Schubert, H. Reetz, C. Görke, O. Kilo, M. Borchardt,G. Mechanical loss, creep, diffusion and ionic, Journal of the European Ceramic Society 20 (2000) 285–296.

[91] Iguchi, F. Endo, Y. Ishida, T. Yokobori, T. Yugami, H. Otake, T. Kawada, T. Mizusaki,J. Oxygen partial pressure dependence of creep on yttria-doped ceria ceramics, Solid State Ionics 176 (2005) 641–644.

[92] Grahl-Madsen, L. Larsen, P. Bonanos, N. Engell, J. Linderoth,S. Mechanical strength and electrical conductivity of Ni–YSZ cermets fabricated by viscous processing, Journal of Materials Science 41 (2006) 1097–1107.

[93] Johnson, J. Qu, J. Effective modulus and coefficient of thermal expansion of Ni–YSZ porous cermets, Journal of Power Sources 181 (2008) 85–92.

[94] Pihlatie, M. Ramos, T. Kaiser, A. Testing and improving the redox stability of Ni-based solid oxide fuel cells, Journal of Power Sources 193 (2009) 322–330.

[95] Malzbender, J. Wakui, T. Steinbrech, R. Curvature of planar solid oxide fuel cells during sealing and cooling of stacks, Fuel Cells 6 (2006) 123–129.

[96] Sun, B. Rudkin, R. Atkinson, A. Effect of Thermal Cycling on Residual Stress and Curvature of Anode-Supported SOFCs, Fuel Cells, 2009.

[97] J. Malzbender, R. Steinbrech, L. Singheiser, Failure probability of solid oxide fuel cells, in: Ceramic Engineering and Science Proceedings, vol. 26, American Ceramic Society, pp. 293–298.

[98] Biswas, S. Nithyanantham, T. Saraswathi, N. Bandopadhyay, S. Evaluation of elastic properties of reduced NiO–8YSZ anode-supported bi-layer SOFC structures at elevated temperatures in ambient air and reducing environments, Journal of Materials Science 44 (2009) 778–785.

[99] Faes, A. Frandsen, H.L. Kaiser, A. Goldstein, D.R. Pihlatie, M. Curvature and strength of Ni–YSZ solid oxide half-cells after redox treatments, Journal of Fuel Cells Science and Technology (2010) 7.

[100] Malzbender, J. Steinbrech,R. Threshold fracture stress of thin ceramic components, Journal of the European Ceramic Society 28 (2008) 247–252.

[101] Lara-Curzio, E. Radovic, M. Trejo, M. Cofer, C. Watkins, T. More,K. Effect of thermal cycling and thermal aging on the mechanical properties of, and residual stresses in, Ni–YSZ/YSZ bi-layers, Advances in Solid Oxide Fuel Cells II 27 (2007) 383–391.

[102] Withey, E. Petorak, C. Trice, R. Dickinson, G. Taylor, T. plasma-sprayed composite coatings for increased creep resistance, Journal of the European Ceramic Society 27 (2007) 4675–4683.

[103] Murray, E.P. Tsai, T. Barnett, S.A. Oxygen transfer processes in (La, Sr)MnO_3/Y_2O_3-stabilized ZrO_2 cathodes: an impedance spectroscopy study, Solid State Ionics 110 (1998) 235–243.

[104] Adler, S. Factors governing oxygen reduction in solid oxide fuel cell cathodes, Chemical Reviews 104 (2004) 4791–4844.

[105] Tai, L.W. Nasrallah, M.M. Anderson, H.U. Sparlin, D.M. Sehlin, S.R. Structure and electrical properties of $La_{1-x}Sr_xCo_{1-y}Fe_yO_3$. Part 1. The system $La_{0.8}Sr_{0.2}Co_{1-y}Fe_yO_3$, Solid State Ionics 76 (1995) 259–271.

[106] Tai, L.W. Nasrallah, M.M. Anderson, H.U. Sparlin, D.M. Sehlin, S.R. Structure and electrical properties of $La_{1-x}Sr_xCo_{1-y}Fe_yO_3$. Part 2. The system $La_{1-x}Sr_xCo_{0.2}Fe_{0.8}O_3$, Solid State Ionics 76 (1995) 273–283.

[107] Xu, Q. Huang, D. Zhang, F. Chen, W. Chen, M. Liu,H. Structure, electrical conducting and thermal expansion properties of $La_{0.6}Sr_{0.4}Co_{0.8}Fe_{0.2}O_{3-\delta}$–$Ce_{0.8}Sm_{0.2}O_{2-\delta}$ composite cathodes, Journal of Alloys and Compounds 454 (2008) 460–465.

[108] Kleveland, K. Orlovskaya, N. Grande, T. Moe, A.M.M. Einarsrud, M.-A. Breder, K. Gogotsi,G. Ferroelastic behavior of $LaCoO_3$-based ceramics, Journal of the American Ceramic Society 84 (2001) 2029–2033.

[109] Pathak, S. Kuebler, J. Payzant, A. Orlovskaya, N. Mechanical behavior and electrical conductivity of $La_{1-x}Ca_xCoO_3$ ($x = 0$, 0.2, 0.4, 0.55) perovskites, Journal of Power Sources 195 (2010) 3612–3620.

[110] Routbort, J.L. Goretta, K.C. Cook, R.E. Wolfenstine, J. Deformation of perovskite electronic ceramics – a review, Solid State Ionics 129 (2000) 53–62.

[111] Lein, H. Wiik, K. Einarsrud, M. Grande, T. Lara-curzio, E. High-temperature creep behavior of mixed conducting $La_{0.5}Sr_{0.5}FeCo_xO_{3-\delta}$ ($0.5 \leq x \leq 1$) materials, Journal of the American Ceramic Society 89 (2006) 2895–2898.

[112] Skarmoutsos, D. Tsoga, A. Naoumidis, A. Nikolopoulos, P. solid oxide fuel cells, Solid State Ionics 135 (2000) 439–444.

[113] Malzbender, J. Wessel, E. Steinbrech, R. Reduction and re-oxidation of anodes for solid oxide fuel cells, Solid State Ionics 176 (2005) 2201–2203.

[114] Minh, N. Takahashi, T. Science and Technology of Ceramic Fuel Cells, Elsevier, 1995.

[115] Tietz, F. Thermal expansion of SOFC materials, Ionics 5 (1999) 129–139.

[116] Guan, X. Zhou, H. Wang, Y. Zhang, J. Preparation and properties of Gd^{3+} and Y^{3+} co-doped ceria-based electrolytes for intermediate temperature solid oxide fuel cells, Journal of Alloys and Compounds 464 (2008) 310–316.

[117] Zheng, Y. Wu, L. Gu, H. Gao, L. Chen, H. Guo, L. The effect of Sr on the properties of Y-doped ceria electrolyte for IT-SOFCs, Journal of Alloys and Compounds (2009).

[118] Pratihar, S. Dassharma, A. Maiti,H. Properties of Ni/YSZ porous cermets prepared by electroless coating technique for SOFC anode application, Journal of Materials Science 42 (2007) 7220–7226.

[119] Meinhardt, K. Kim, D.-S. Chou, Y.-S. Weil, K. Synthesis and properties of a barium aluminosilicate solid oxide fuel cell glass–ceramic sealant, Journal of Power Sources 182 (2008) 188–196.

[120] Dutta, A. Mukhopadhyay, J. Basu, R. Combustion synthesis and characterization of LSCF-based materials as cathode of intermediate temperature solid oxide fuel cells, Journal of the European Ceramic Society 29 (2009) 2003–2011.

[121] Huang, B. Malzbender, J. Steinbrech, R. Singheiser, L. Mechanical properties of $La_{0.58}Sr_{0.4}Co_{0.2}Fe_{0.8}O_{3-\delta}$ membranes, Solid State Ionics 180 (2009) 241–245.

[122] Malzbender, J. Steinbrech, R. Fracture test of thin sheet electrolytes for solid oxide fuel cells, Journal of the European Ceramic Society 27 (2007) 2597–2603.

[123] Pihlatie, M. Kaiser, A. Larsen, P. Mogensen, M. Dimensional behaviour of Ni–YSZ anode supports for SOFC under redox cycling conditions, ECS Transactions (2007) 1501–1510.

[124] Faes, A. Frandsen, H.L. Kaiser, A. Pihlatie, M. Strength of anode-supported solid oxide fuel cells, Fuel Cells 11 (5) (2010) 682–689.